


Moiré fractals in twisted graphene layers

 Deepanshu Aggarwal , Rohit Narula, and Sankalpa Ghosh 

Department of Physics, Indian Institute of Technology Delhi, Hauz Khas, New Delhi 110016, India

 (Received 26 June 2023; revised 8 February 2024; accepted 9 February 2024; published 1 March 2024)

Twisted bilayer graphene (TBLG) subject to a sequence of commensurate external periodic potentials reveals the formation of moiré fractals (MFs) that share striking similarities with the central place theory of economic geography, thus uncovering a remarkable connection between twistrionics and the geometry of economic zones. MFs arise from the self-similarity of the emergent hierarchy of Brillouin zones (BZs), forming a nested subband structure within the bandwidth of the original moiré bands. We derive the fractal generators for TBLG under these external potentials and explore their impact on the hierarchy of the BZ edges and the wave functions at the Dirac point. By examining realistic supermoiré structures and demonstrating their equivalence to MFs with periodic perturbations under specific conditions, we establish MFs as a general description for such systems. Furthermore, we uncover parallels between the modification of the BZ hierarchy and magnetic BZ formation in Hofstadter's butterfly, allowing us to construct an incommensurability measure for MFs versus twist angle. The resulting band structure hierarchy bolsters correlation effects, pushing more bands within the same energy window for both commensurate and incommensurate TBLG.

 DOI: [10.1103/PhysRevB.109.125302](https://doi.org/10.1103/PhysRevB.109.125302)

I. INTRODUCTION

Fractals are fascinating structures that are found in both natural and abstract forms, from the intricate patterns of Romanesco broccoli to the complex geometry of the Mandelbrot set [1,2]. Iterated function systems (IFSs) are a powerful tool for generating fractals, with many unusual geometries emerging as attractors [3], e.g., Koch curves [4]. Iterated fractals (IFs) involve applying a generator recursively to a starting shape—an initiator. Particularly interesting are IFs generated by

$$x^2 + \beta x - (L_N - \beta^2)/3 = 0, \quad (1)$$

where for $\beta \in \mathbb{N}$, if it has a discriminant $\mathcal{D} \in \mathbb{Z}$, then $L_N \in \mathbb{N}$ generate a triangular lattice with integral coordinates [5] [Fig. 1(a)].

In this paper, we show that Eq. (1) describes an emergent fractality when commensurate or incommensurate moiré patterns in (twisted bilayer graphene) TBLG [7–43] are subjected to a sequence of superlattice periodic potentials (SOPPs) [Fig. 1(b)], having the same moiré periodicity as structures on which they are applied, but twisted by an angle restoring commensuration. The sequence of iterated edges of the first Brillouin zone (FBZ) forms a fractal (Figs. 2 and 4) with dimensions determined by L_N (the number of unit cells in a newly formed BZ fitting a unit cell of the preceding BZ at each iteration).

The emergent fractality of Eq. (1), dubbed the moiré fractal (MF), resembles the hierarchy and fractality of economic geography's central place theory (CPT) as pioneered by Christaller and Baskin [44–46] and Lösch and Woglom [47], which terms L_N as Löschian numbers [48]. This connection emerges when densely packed hexagonal trade areas centered on settlements are multiply stacked with trade areas representing smaller settlements [46,47,49–54] [Fig. 1(c)]. The MF

dimension (D_f) provides quantitative information about the band structure of realistic supermoiré structures (SMSs), e.g., multiple graphene or hexagonal boron nitride (hBN)-graphene layers [55–60]. Further, we establish an analogy with Hofstadter's butterfly (HB) [61,62] explaining the topological quantization of Hall conductivity [63,64], thus formulating an incommensuration measure for moiré structures.

II. THE HAMILTONIAN AND EMERGENT FRACTALITY IN MOIRÉ FRACTALS

The rapid progress in the fabrication of two-dimensional (2D) layered materials, e.g., TBLG, has stimulated interest in the effect of substrates [65–68]. Such materials experience an external potential with a moirélike periodicity when placed on substrates with matching [69] or mismatched layers [70,71], which may be modeled as perturbations to the Hamiltonian of TBLG (H_{TBLG}) via external periodic potentials [71–73]. H_{TBLG} subjected to SOPP at the j th iteration is

$$H_j = \begin{bmatrix} \hat{h}_k(\theta/2) + \sum_{i=1}^j V_i(\mathbf{r}) & T(\mathbf{r}) \\ T^\dagger(\mathbf{r}) & \hat{h}_k(-\theta/2) + \sum_{i=1}^j V_i(\mathbf{r}) \end{bmatrix}, \quad (2)$$

where $\hat{h}_k(\theta) = v_F \boldsymbol{\sigma}_\theta \cdot (\hat{\mathbf{k}} - \mathbf{K}^\theta)$ [74] describes single-layer graphene (SLG) rotated by θ , v_F [75] is the Fermi velocity, and \mathbf{K}^θ is the rotated, right-valley Dirac point. The transformed Pauli matrices $\boldsymbol{\sigma}_\theta = e^{-i\sigma_z \theta/2} (\sigma_x, \sigma_y) e^{i\sigma_z \theta/2}$ provide the rotation. The expressions for the interlayer hopping matrices $T(\mathbf{r})$ [11,76–78] are given in Appendix F. The external potential $V_j(\mathbf{r})$ exhibits a periodicity: $V_j(\mathbf{r} + n_1 \mathbf{t}_1^{(j)} + n_2 \mathbf{t}_2^{(j)}) = V_j(\mathbf{r})$, where the primitive vectors (PVs) $\mathbf{t}_{1,2}^{(j)} = [\mathcal{R}(\theta)] \mathbf{a}_{1,2}^{(j-1)}$. $\theta = \theta_r$ is the twist between the moiré pattern and the moiré external potential (mEP), leading to commensuration between mEP at each j th iteration and TBLG with all potentials up to the $(j-1)$ th iteration. $\mathcal{R}(\theta_r)$ denotes a 2D

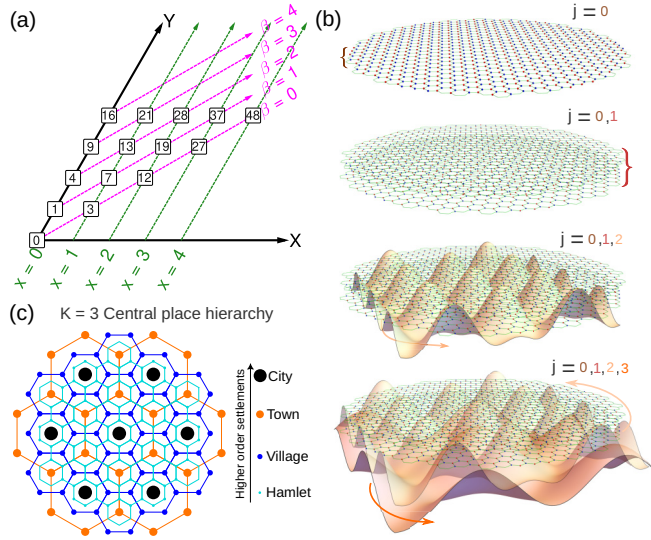


FIG. 1. (a) L_N , β , and x over triangular coordinates (the axes are 60° with respect to each other). The intersection of β (magenta) and x (green) lines identify the intersection points $(x, y = x + \beta)$ at which L_N exists. (b) The real-space creation of each iteration: TBLG is created by stacking graphene layers with the top layer being the zeroth iteration $j = 0$ and the bottom layer being the next $j = 1$. The iterations $j = 2, 3, \dots$ are created by applying the z -independent external periodic potentials identically to both the graphene layers. (c) The $K = 3$ CPT hierarchy (since a hexagon of each layer encloses three hexagons of an adjacent layer) where each layer corresponds to a particular order of settlement [6]. L_N is analogous to K .

rotation matrix at these commensurate angles. The condition for commensuration under such rotation maps an integer pair $\mathbf{n} = \{n_1, n_2\}$ to $\mathbf{m} = \{m_1, m_2\}$ (Appendix D). The integral solutions m_1, m_2, n_1 , and n_2 satisfy the necessary and sufficient condition when the matrix elements assume only rational values [12,79], leading to a set of Diophantine equations (Appendix D) whose solutions provide the PV of the commensurate supercell, i.e., $\{\mathbf{a}_1^{(2)}, \mathbf{a}_2^{(2)}\}$ in terms of the PV of the preceding structure.

For the SOPP of Fig. 1, $V_1(\mathbf{r}) = 0$ at $j = 1$, H_1 in (2) becomes H_{TBLG} , while the potentials for $j \geq 2$ are nonzero. For $j = 2$, $V_2(\mathbf{r})$ is periodic with $\mathbf{t}_{1,2}^{(2)} = [\mathcal{R}(\theta_r)]\mathbf{a}_{1,2}^{(1)}$ where $\mathbf{a}_{1,2}^{(1)}$ are the PV of commensurate TBLG. On repeating this procedure, the commensuration of $V_j(\mathbf{r})$ and the structure up to the $(j - 1)$ th-level is spanned by $\{\mathbf{a}_1^{(j)}, \mathbf{a}_2^{(j)}\}$. We demonstrate this via a cosine potential V_0 with only six Fourier components (Appendix F). The intrinsic Coulomb interactions can be modeled using such an on-site mEP having the same periodicity as the moiré pattern [80–83] as a starting *ansatz* for a self-consistent calculation. For the first iteration of $V_2(\mathbf{r})$ (Appendix G, Figs. 11–15) various SMSs, e.g., trilayer graphene [55–57,84–86], four-layer graphene [58,59,87,88], and trilayer hBN-G-hBN [60,89], are modeled by (2), representing an MF and a weak periodic perturbation whose details depend on the system considered. V_0 can be controlled by [90] the interlayer separation (d) and the interlayer bias (V_{STM}), essentially the bias applied to a scanning tunneling microscope (STM) tip, i.e., $|V_{\text{STM}}| \approx 20 - 500$ meV [91,92]. Typically, $V_0 \sim 1.2$ meV for $|V_{\text{STM}}| = 45$ meV given $d \sim 1$ nm.

Each commensuration of either TBLG or TBLG plus the mEPs gives (Appendix D)

$$A_{\text{FBZ}}^{(j-1)} / A_{\text{FBZ}}^{(j)} = L_N = p_1^2 + p_2^2 + p_1 p_2, \quad (3)$$

where $A_{\text{FBZ}}^{(j)} = |\mathbf{b}_1^{(j)} \times \mathbf{b}_2^{(j)}|$ represents the area of the first BZ at j th iteration and $\mathbf{a}_i^{(j)} \cdot \mathbf{b}_k^{(j)} = 2\pi \delta_{ik} \forall i, k = 1, 2$ and $p_1(p, q), p_2(p, q) \in \mathbb{Z}^+$ (Appendix D, Fig. 8), with p, q being coprime numbers. For a hexagonal lattice, $p_2 = p_1 + \beta$ such that L_N with $\beta = 0$ lie on the line $X = Y$ while the numbers with $\beta > 0$ lie on lines parallel to $X = Y$ [Fig. 1(a)], converting Eq. (3) into Eq. (1), therefore making each L_N lie at an intersection of the x and β rays [Fig. 1(a)].

For each L_N and β , the corresponding fractal generator (FG) is generated by applying IFSs to one side of the initiator A_0 [3], i.e., the rotated BZ of SLG (a constituting layer in TBLG) (details in Appendix A). Applying this FG to each arm of A_0 generates the edges of successive BZs, continuing the recursive process to produce a sequence of BZs.

The hierarchical construct in CPT, i.e., L_N exhibits successively smaller regions within a trade area at each stage. Number theory [93] identifies conditions for L_N fulfilling Eq. (1). This connection between the CPT lattice partition and Eq. (1) facilitates the systematic determination of lattice coordinates for economic zones and the corresponding FG responsible for CPT associated with L_N . For TBLG in the presence of specific mEPs, we begin with the transformation mappings of the FGs for $q = 3, p = 1$ and $q = 2, p = 1$, corresponding to $\theta \sim 21.79^\circ$ [94] and $\theta \sim 32.20^\circ$. $D_f = \ln(n_c) / \ln(s)$ for the attractor A [1], where $s = \sqrt{L_N}$ is the contractivity factor (Appendix A, Fig. 5).

III. IMPLICATIONS OF THE ABOVE CONSTRUCTION FOR THE BAND STRUCTURE

Figures 2(a1) and 2(b1) display the superimposed BZs for $j = 1, 2, 3$ corresponding to the hierarchical mEP applied to two commensurate structures at $\theta = \theta_r \sim 21.79^\circ$ and $\theta = \theta_r \sim 32.20^\circ$. The FG shape is shown in the next column. For both, it is applied alternately outside and inside the edges of the initiators [red dashed lines, Figs. 2(a2) and 2(b2)], exhibiting emergent fractality with $D_f = 1.129$ and $D_f = 1.255$. The real-space fractals corresponding to $q = 3, p = 1$ are shown in Appendix B, Fig. 7. The reciprocal lattice vectors (RLV) magnitudes for $i = 1, 2$ form a Cauchy sequence [95] as $\lim_{j \rightarrow \infty} \{ \frac{|b_i^{\pm\theta/2}|}{s^{(j-1)}} \} \rightarrow 0$ whose convergence rates depend on q, p (solid blue and red lines in the insets of Fig. 2).

The commuting translation operators (TOs) at the j th iteration with the Hamiltonian (2) for the rotated mEP with PV $\mathbf{a}_1^{(j)} = p_1 \mathbf{a}_1^{(j-1)} + p_2 \mathbf{a}_2^{(j-1)}$ and $\mathbf{a}_2^{(j)} = -p_2 \mathbf{a}_1^{(j-1)} + (p_1 + p_2) \mathbf{a}_2^{(j-1)}$ differ from the PV at the $(j - 1)$ th iteration. They satisfy $\hat{T}_{\mathbf{a}_1^{(j)}} \hat{T}_{\mathbf{a}_2^{(j)}} = \hat{T}_{\mathbf{a}_2^{(j)}} \hat{T}_{\mathbf{a}_1^{(j)}}$, leading to a large real-space supercell with a more squeezed BZ scaled by s [Figs. 2(a1) and 1(b1)], conventionally termed as a *minizone* [68,97]. This has similarities with the HB problem [61,98,99], where the magnetic TOs do not commute. Consequently, for a time reversal (TR) symmetric, commensurate TBLG in a rotated mEP, we

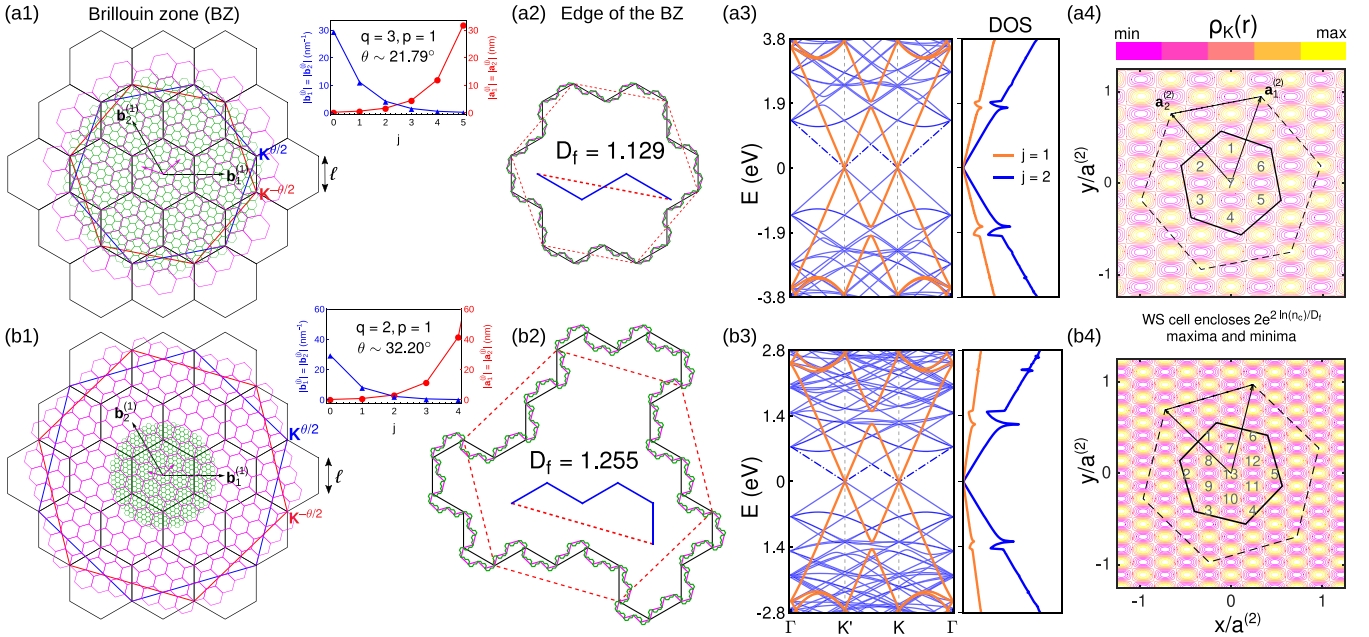


FIG. 2. (a1), (b1) The BZ for $j = 1$ (black), 2 (magenta), and 3 (green), where $\{\mathbf{b}_1^{(j)}, \mathbf{b}_2^{(j)}\}$ are the reciprocal lattice primitive vectors for $j = 1$. (a2), (b2) The fractal structures at the BZ edges. The dashed red hexagon represents the initiator, i.e., the BZ of SLG rotated by $\theta/2$. The solid blue lines outline the fractal structures' outer boundary. The generators (inside) attach alternately to the initiator, forming the fractal structure. The copies of the BZ at each iteration are added such that they overlap with the BZ of SLG [red solid lines in (a1) and (b1)] and these overlaps lead to IFs. The insets between (a1), (a2) and (b1), (b2) display reciprocal and real-space lattice vectors for $q = 3, p = 1$ and $q = 2, p = 1$, respectively. The shift between the Dirac points is equal to the hexagon's side length for $q = 3, p = 1$, and twice its side for $q = 2, p = 1$. (a3), (b3) The band structures for $V_0 = 1.2$ meV and the DOS (with a Gaussian smearing of 0.002 meV). (a4), (b4) $\rho_{nk}(\mathbf{r})$ of the lowest conduction band (dashed-dotted line) at the Dirac point (see text, Appendix H).

define a dimensionless incommensurability measure [100],

$$\frac{\Delta A(\theta)}{A_{\text{FBZ}}^{(j-1)}} = \left(1 - \frac{A_{\text{FBZ}}^{(j-1)}/A_{\text{FBZ}}^{(j)}}{A_{\text{FBZ}}^{(j-1)}/A_{\text{FBZ}}^{(j)}} \right), \quad (4)$$

where $[\dots]$ denotes the greatest integer function.

Following Refs. [11,96,101] for any θ between TBLG and mEP [Fig. 2(b1)], $\mathbf{b}_{1,2}^{(j)}$ of the mBZ are obtained from $\Delta \mathbf{K} = \mathbf{K}^{\theta/2} - \mathbf{K}^{-\theta/2}$. These definitions coincide for $p = 1$ and odd integer q with the lattice vectors giving the hexagonal BZ side length as $\ell = |\frac{2\mathbf{b}_1^{(j)} + \mathbf{b}_2^{(j)}}{3}|$ [Figs. 2(a1) and 2(b1)], such that $A_{\text{FBZ}}^{(j-1)}/A_{\text{FBZ}}^{(j)} = L_N \Rightarrow \Delta A = 0$, corresponding to the blue points in Fig. 3.

For generic (q, p) , the two definitions do not coincide and $\Delta A/A_{\text{FBZ}}^{(j-1)}$ shifts upward from the $\Delta A = 0$ line by differing amounts (Fig. 3). The angles corresponding to the minima of the V regions are commensurate angles where the ratio becomes rational (Appendix E). Figure 3 (inset) shows that these minima are not vertically collinear: the lateral shift is $\sim 0.002^\circ$.

Figures 2(a3) and 2(b3) display the band structures for $j = 1$ (H_{TBLG}) and $j = 2$ in the presence of mEP $V_2(\mathbf{r})$ and the density of states (DOS). Precisely, $2(2e^{2\ln(n_c)/D_f} - 1)$ (Appendix C) bands, per Eq. (3), populate the band gap of 6.38 eV for $\theta_r \sim 21.79^\circ$ and 5.04 eV for $\theta_r \sim 32.20^\circ$ between the two lowest bands at the Γ point, without the mEP. Additional bands at K and K' occupy an even narrower range within the band gap versus the Γ point, with the two lowest bands

meeting at the Dirac point. Figures 2(a4) and 2(b4) provide the probability density $\rho_{nk} = |\psi_{nk}|^2$ of the Bloch wave functions obtained by diagonalizing (2) at the Dirac point. The number of maxima and minima within the Wigner-Seitz cell for the lowest conduction band is $2e^{2\ln(n_c)/D_f}$ (Appendix H). The MFs in (2) therefore provide precise control over the number of in-gap states given D_f by changing θ_r , which is in contrast to other such methods for small-angle TBLG [102–104] and SMSs [56,105].

For magic-angle TBLG (MATBLG) [8,11,106,107], the flat bands facilitate various correlated phases [22,23,108–115]. The FGs apply alternately outside and inside the edges of their initiators, which are the mBZ of MATBLG [red dashed lines in Figs. 4(a) and 4(b)], also showing the superimposed BZs for $j = 1, 2, 3$ at the first magic angle $\theta \sim 1.05^\circ$. For Fig. 4(a), $\theta_r \sim 13.17^\circ$ and $D_f = 1.093$, while for Fig. 4(b) $\theta_r \sim 21.79^\circ$ and $D_f = 1.129$. The change in D_f and L_N alters the number of bands pushed towards the Fermi level E_F at the Γ point within a band gap of ~ 13.76 meV for MATBLG, preserving the emergent fractality similar to commensurate structures. An additional $2(e^{2\ln(n_c)/D_f} - 1)$ inner bands again exhibit significantly reduced curvature compared to the original flat bands. Figure 10 verifies that TBLG's renormalized v_F remains indifferent to the presence of hierarchical mEP, despite the shift in E_F . The Hamiltonian (2) ignores lattice relaxation effects, namely, the variations in the interlayer hopping amplitudes in the AA-BB- and AB-BA-rich regions. Their [24,28,101,116] inclusion doesn't alter this emergent fractality linked to the band structures (Appendix F, Fig. 9).

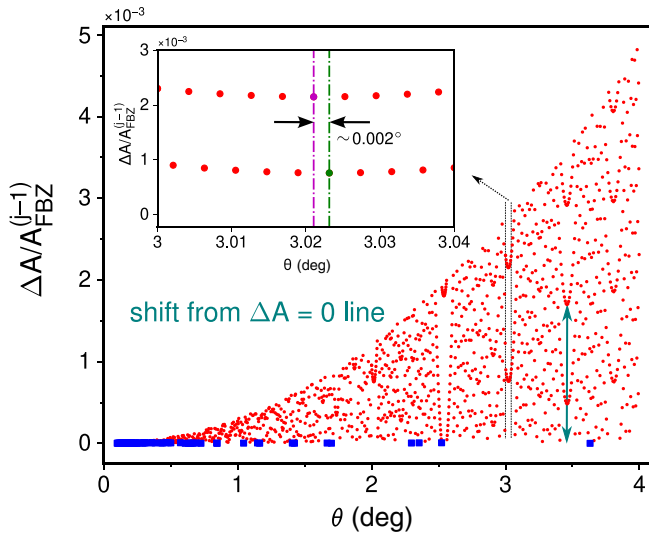


FIG. 3. $\frac{\Delta A}{A_{\text{FBZ}}^{(j-1)}}$ vs θ : The blue rectangles represent commensurate (closest) angles for odd q and $p = 1$. The first BZ area for incommensurate angles is determined using moiré vectors [96]. The inset confirms the absence of the apparent multivaluedness in the lowest values of the V regions between the dashed lines, with a separation of $\sim 0.002^\circ$.

Much like how the recursive stacking of nets in CPT leads to a proliferation of smaller settlements within a designated area, the recursive mEP in TBLG produce an expanding count of electronic bands within a defined energy range, thereby amplifying correlation effects, with both scenarios characterized by L_N . The impact of this band engineering and emergent fractality on electronic correlation can be understood through the Hubbard parameter ratio between the interaction energy U

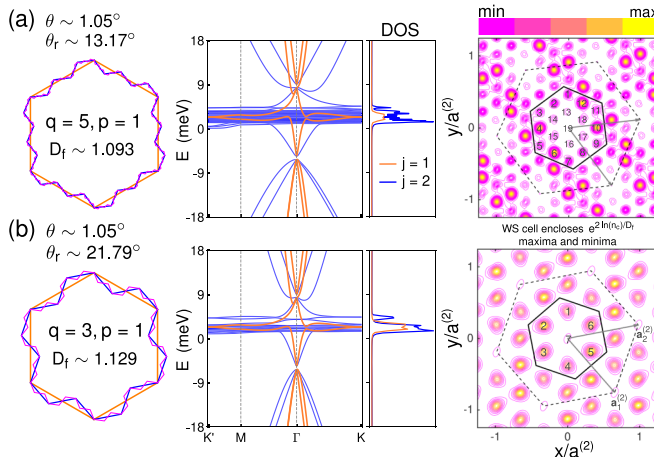


FIG. 4. The band structures at $\theta_r \sim 21.79^\circ$ in (a) and $\theta_r \sim 13.17^\circ$ in (b) along $K' - M - \Gamma - K$. The twist between the layers is the first magic angle $\theta \sim 1.05^\circ$. The interlayer hopping parameters: $t_{\text{AA/BB}} = t_{\text{AB/BA}} = 110$ meV (Appendix F) and $V_0 = 1.2$ meV. Left to right: The emergent fractal structure in reciprocal space, 2D band structure: orange (blue) bands without (with) mEP, the DOS, and the spatial profiles of $\rho_K(\mathbf{r})$ of the lowest conduction band with $j = 2$. Changing θ_r from (b) to (a) modifies D_f , shifting more bands towards E_F .

and the bandwidth t_W (the difference between the band maxima and minima). Since in (2), H_{TBLG} and the rotated MEP have different translational symmetries, $\lim_{V_0 \rightarrow 0} \frac{U}{t_W}$ doesn't yield the same ratio for pristine TBLG [23]. However this ratio depends on mEP V_0 when E_F lies within the flat band, $\frac{U}{t_W} \gg 1$. Under an mEP, $U \rightarrow \frac{U}{s}$, for $U = e^2 \theta / 4\pi \kappa \epsilon_0 a$ without any mEP (Appendix I), where e is electronic charge and $\kappa = 4$. However, the closest flat band near E_F experiences a significantly larger reduction in bandwidth versus s , e.g., in Fig. 4(a), the bandwidth decreases from ~ 6 meV to ~ 0.23 meV (Fig. 16), leading to ~ 9 times increase in $\frac{U}{t_W}$ versus MATBLG. The effective mass m^* scales as \sqrt{n}/v_F at E_F , increasing with the superlattice density n scaled by L_N ; so does DOS.

IV. CONCLUSION

In summary, we have introduced MFs in TBLG subjected to a sequence of commensurate, rotated external potentials, thus establishing a framework for studying their properties and drawing parallels between emergent fractality in sp^2 carbons and the agglomeration of CPT trade zones. The band structure of several SMSs can be understood via MFs and a weak perturbation enabling insertion of a controlled number of in-gap bands determined by D_f . We analyzed the restructuring of the moiré unit cell and established an incommensurability measure, linking it to correlation effects and D_f . The MFs remained robust despite corrugation effects.

Amidst the emerging domain of SMSs, including trilayer [57,84–86], tetralayer [87,117–119], and pentalayer graphene [88,120], scenarios where slight rotations of SLG interact with thin graphitic crystals [121,122], dissimilar layers like encapsulated SLG and bilayer graphene between hBN layers [60,89,123,124], and moiré lattices in photonic crystals [125] and ultracold atom systems [126–128], we've provided a general framework allowing such systems to be understood as MFs under weak perturbations.

The increase in the number of MF bands near E_F can be detected via differential tunneling conductance measurements for the corresponding SMS under suitable conditions (Appendix J) as was done for quasicrystals with a Penrose tiling [129]. Real-space scanning probes like the quantum twisting microscope [94] offer another approach by gating the vdW device on a rotating platform, thereby enabling a rotated moiré effect. The optical conductivity, absorption coefficient, and the photocurrent which depend on the interband transitions [43,130,131], and experiments analogous to cryogenic nanoscale photovoltage measurements [132] (Appendix J) on hBN-encapsulated TBLG may also exhibit the MF signatures. Future research will investigate MF symmetry [133], implications for strong-correlation physics, extension to external potentials without common moiré periodicity [134–136], any nontrivial topological properties embedded in our incommensuration measure, and the possibility of fractality in moiré quasicrystals [57,137–140].

ACKNOWLEDGMENTS

S.G. is supported by MTR/2021/000513 funded by Science and Engineering Research Board, Department of Science and Technology, Govt. of India. D.A. is supported by a UGC fellowship.

TABLE I. Each commensuration is characterized uniquely by a pair of coprime integers (q, p) . The L schian number L_N and the FG are obtained by identifying the number of sides n_c in the FG. The fractal dimension (D_f) corresponding to the various q, p are calculated using L_N and n_c [141]. The outer boundary of the minizones superposed over the FBZ of SLG is generated by attaching the FG on a hexagonal initiator.

θ	q	p	L_N	β	n_c	Generator	D_f
21.79�	3	1	7	1	3		1.129
32.20�	2	1	13	2	5		1.255
13.17�	5	1	19	1	5		1.093
38.21�	5	3	7	1	3		1.129
17.90�	11	3	31	4	9		1.280
:							

APPENDIX A: THE PROPERTIES OF THE FRACTAL GENERATORS (FG)

Here we provide details of the transformation mappings for FGs corresponding to $q = 3, p = 1$ and for $q = 2, p = 1$, respectively, whose effect on the band structure was shown in Fig. 2 of the main text. More examples with additional discussion are provided in Table I. The first case corresponds to the commensurate angle $\theta \sim 21.79^\circ$, which has recently been explored experimentally for pristine TBLG [94]. The number of contraction mappings, that is, an associated cardinal number n_c of IFS $W = \{w_n : n = 1, 2, \dots, n_c\}$ [3] is obtained for each L_N and β . In this case, L_N is found to be 7 and lie at the intersection of $x = 1$ and $\beta = 1$ lines as shown in Fig. 1(a) of the main text. Correspondingly, n_c of the IFS comes out to be 3, giving $W = \{w_1, w_2, w_3\}$, where $w_1 = \mathcal{R}(-\phi_1)\frac{\mathcal{I}}{s}$, $w_2 = \mathcal{R}(\phi_2)\frac{\mathcal{I}}{s} + w_1$, $w_3 = w_1 + w_2$ with $s = \sqrt{L_N} = |\mathbf{b}_{1/2}^{(j-1)}|/|\mathbf{b}_{1/2}^{(j)}|$ being the contractivity factor and \mathcal{I} is a 2×2 identity matrix. For $\{p_1, p_2, s\} = \{1, 2, \sqrt{7}\}$, $\phi_1 = \cos[-1](\frac{2p_1+p_2}{2s})$ and $\phi_2 = \frac{\pi}{3} - \phi_1$. D_f of the attractor A is obtained using L_N as $D_f = \ln(n_c)/\ln(s)$ [1].

To understand w_n 's action on one of the sides of A_0 (BZ of SLG), rotated clockwise with the angle $\theta/2 \sim 10.89^\circ$, and represented by reciprocal lattice vector $\mathbf{u} = \frac{1}{3}(2\mathbf{b}_1^{-\theta/2} + \mathbf{b}_2^{-\theta/2})$ (see Fig. 5), where $\mathbf{b}_1^{-\theta/2}$ and $\mathbf{b}_2^{-\theta/2}$ are the two reciprocal lattice vectors of the rotated graphene layers, we note that w_1 shortens $|\mathbf{u}|$ by $s = \sqrt{7}$ times and rotates \mathbf{u} clockwise by an angle $\cos[-1](2/\sqrt{7})$, providing the first side

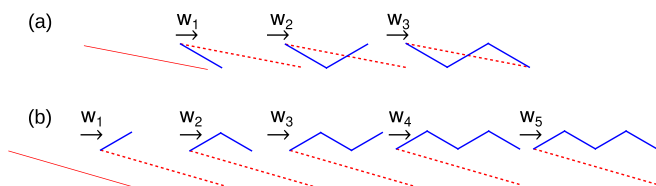


FIG. 5. (a) The stepwise creation of the FG for $L_N = 7$ with $q = 3$ and $p = 1$, and (b) $L_N = 13$ with $q = 2$ and $p = 1$. The red dashed line is the side \mathbf{u} of A_0 as defined in Appendix A.

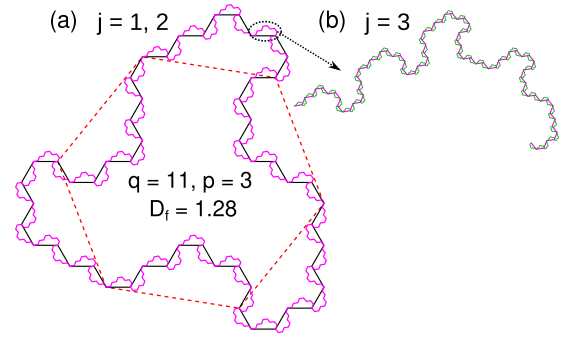


FIG. 6. (a) The fractal corresponding to one more entry in Table I, where $q = 11$ and $p = 3$, having $L_N = 31$ with $\beta = 4$ at an angle of $\theta_r = 17.89^\circ$ for $j = 1, 2$. (b) The fractal corresponding to the iteration $j = 3$.

of the FG, namely, \mathbf{u}_1 . Similarly, the successive mappings are $\mathbf{u}_{2,3} = w_{2,3}\mathbf{u}$. The second case mentioned in the main text, corresponds to the commensuration $\theta \sim 32.20^\circ$ with $q = 2$ and $p = 1$, for which $L_N = 13$ and $n_c = 5$. Considering the side of the initiator to be identical to \mathbf{u} , the mappings become $w_1 = \mathcal{R}(\phi_1)\frac{\mathcal{I}}{s}$; $w_2 = \mathcal{R}(-\phi_2)\frac{\mathcal{I}}{s} + w_1$; $w_3 = w_1 + w_2$; $w_4 = w_2 + w_3$; $w_5 = \mathcal{R}(-(\frac{\pi}{3} + \phi_2))\frac{\mathcal{I}}{s} + w_4$, where $p_1 = 1, p_2 = 3$, and $s = \sqrt{13}$. The application of the contraction mappings w_n 's for the first two entries in Table I are shown in Fig. 5.

The other FGs in Table I, such as for $q = 5$ and $p = 3$, lead to the same values $L_N = 7$ and $\beta = 1$ as for $q = 3$ and $p = 1$, but the shift between the Dirac points for commensurate TBLG is $\Delta\mathbf{K} = \mathbf{b}_2^c$. However, the FG remains identical to the one for $q = 3$ and $p = 1$. In fact, the mappings for the FGs corresponding to the other values of q being an odd number with $p = 1$ remain the same with an increasing cardinal number n_c . Therefore, the class of commensurate structures with q being an odd number and $p = 1$ associate with the FGs having the same shape but with a different number of sides. If one draws a line that is perpendicular to the red dashed line in Fig. 5(a) which bisects the FG, it exactly cuts it into two pieces with one becoming the other with a rotation of π in the plane containing the FG. In the case of $q = 11$ and $p = 3$, the shift $\Delta\mathbf{K} = \mathbf{b}_2^c$ is the same as for $q = 5$ and $p = 3$ but the FG is asymmetric about the perpendicular bisector. The corresponding FG is shown in Fig. 6. It shows the $j = 1, 2$ -level iterations in (a) and the one for $j = 3$ in (b). Similarly, for $q = 4$ and $p = 1$, the shift in the Dirac points $\Delta\mathbf{K} = 2(2\mathbf{b}_1^c + \mathbf{b}_1^c)/3$ is very different from the previous cases but the FG has a similar shape as for $q = 2$ and $p = 1$, where $\Delta\mathbf{K}$ is identical.

APPENDIX B: THE REAL-SPACE CONSTRUCTION OF THE MOIR  FRACTALS

While the contraction mappings $\{w_1, w_2, w_3, \dots\}$ for a MF in real-space corresponding to a given value of q, p remain identical, the initiator, however, is different. In reciprocal space, the FG is applied to the side of a hexagon of a rotated SLG in the commensurate case, while it's applied to an arm of the moir  BZ for the incommensurate case to obtain the IF.

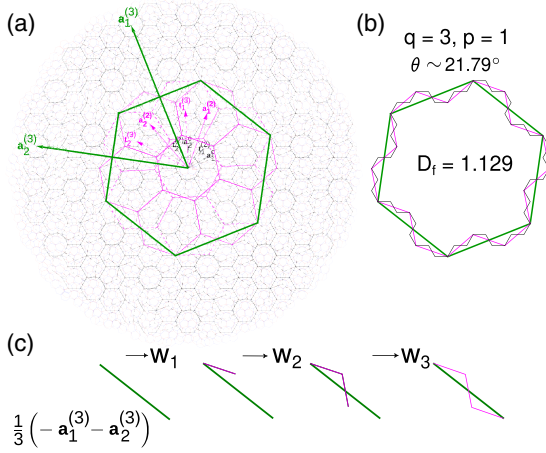


FIG. 7. (a) The real-space structure of commensurate TBLG at $\theta \sim 21.79^\circ$ and two levels of periodic potentials for $j = 2, 3$. The direct-lattice primitive vectors are also shown for each level. (b) The corresponding moiré fractal along the edges of the Wigner-Seitz unit cell at $j = 3$. (c) The initiator, the arm of the hexagon corresponding to $j = 3$, and the FG.

However, the initiator in the real space is the arm of a hexagon which corresponds to the highest-level of iteration of the chosen j values. e.g., Fig. 7(b) shows the MF corresponding to $q = 3$ and $p = 1$. Since the j values considered are 0, 1, 2, 3, the initiator is the side of the hexagon corresponding to the commensurate cell of $j = 3$.

APPENDIX C: THE RELATION OF THE NUMBER OF BANDS WITH THE FRACTAL DIMENSION (D_f)

As given in the main text, the number of bands for $\theta = \theta_r$ within the band gap of the two lowest bands at the Γ point is $4e^{2\ln(n_c)/D_f} - 2$ [see Figs. 2(a3) and 2(b3) of the main text], while for $\theta \neq \theta_r$, the number of bands is $2e^{2\ln(n_c)/D_f} - 2$ (see Fig. 4 in the main text). The dependence of the number of bands on the cardinal number n_c and the fractal dimension D_f is obtained from L_N , which is related to n_c and D_f as

$$D_f = \frac{\ln(n_c)}{\ln(\sqrt{L_N})}. \quad (\text{C1})$$

After some rearrangement, the crucial quantity L_N can be written as

$$L_N = e^{2\ln(n_c)/D_f}. \quad (\text{C2})$$

The number of bands depends upon L_N and, therefore, it depends upon n_c and D_f through (C2).

APPENDIX D: DERIVATION OF EQ. (3) OF THE MAIN TEXT

For a general 2D-Bravais lattice case, the direct lattice PVs of the constituting layers \mathbf{a}_1 and \mathbf{a}_2 are not necessarily orthogonal, i.e., $\mathbf{a}_1 \cdot \mathbf{a}_2 = a_1 a_2 \cos(\phi) \neq 0$ and also $|\mathbf{a}_1| \neq |\mathbf{a}_2|$. Therefore, the general square matrix that maps an integer pair $\mathbf{n} = \{n_1, n_2\}$ to $\mathbf{m} = \{m_1, m_2\}$ is given by

$$\mathbf{m} = \left[\cos \theta_r - \epsilon \frac{(\sigma_z \cos(\phi) a_1 + i \sigma_y a_2)}{a_1 \sin(\phi)} \sin \theta_r \right] \mathbf{n}. \quad (\text{D1})$$

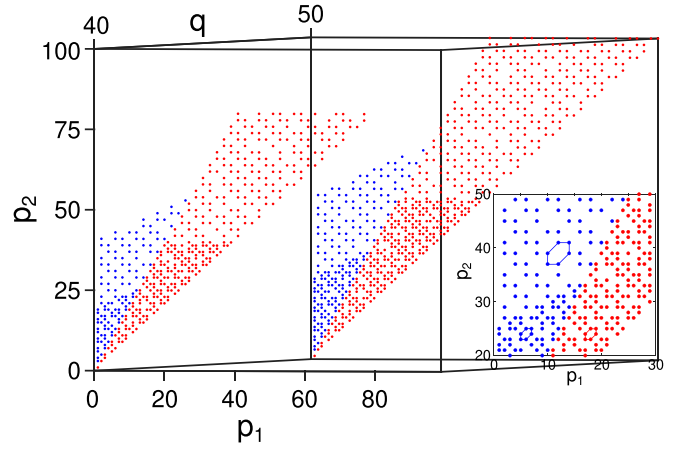


FIG. 8. p_1 vs p_2 for two maximum values of q . Evidently, the points arrange themselves in hexagons and each point is associated with a Löschian number L_N .

Here $\epsilon = \text{sgn}[(\mathbf{a}_1 \times \mathbf{a}_2)_z]$, $a_{1/2} = |\mathbf{a}_{1/2}|$, and ϕ represents the angle between \mathbf{a}_1 and \mathbf{a}_2 . For the present hexagonal case, $|a_1| = |a_2|$ and $\phi = 60^\circ$, the necessary and sufficient condition for the integer solutions m_1, m_2, n_1 , and n_2 demands the matrix elements to assume only rational values [79]. The commensurate angle θ_r then becomes

$$\theta_r(q, p) = 2 \tan^{-1}(p/\sqrt{3}q), \quad (\text{D2})$$

where $q > p > 0$. As $p/q \rightarrow 0$ gives $\theta_r \rightarrow 0$ and $p/q \rightarrow 1$ gives $\theta_r \rightarrow 60^\circ$. The commensurate structures are distinguished on the basis of $\delta = \text{gcd}(p, 3)$ and the direct lattice primitive vectors are

$$\begin{bmatrix} \mathbf{a}_1^c \\ \mathbf{a}_2^c \end{bmatrix} = \begin{bmatrix} p_1 & p_2 \\ -p_2 & p_1 + p_2 \end{bmatrix} \begin{bmatrix} \mathbf{a}_1 \\ \mathbf{a}_2 \end{bmatrix}, \quad (\text{D3})$$

where $p_1 = (3q - p)/\gamma$ and $p_2 = 2p/\gamma$ for $\delta = 3$ and $p_1 = (q - p)/\gamma$ and $p_2 = (q - p)/\gamma$ for $\delta = 1$ and the quantity $\gamma = \text{gcd}[3q + p, 3q - p]$. For both cases $\delta = 1$ and $\delta = 3$, the two elements in the first row, p_1 and p_2 , are positive integers \mathbb{Z}^+ . Corresponding to the direct space PVs \mathbf{a}_1^c and \mathbf{a}_2^c , the reciprocal space PVs \mathbf{b}_1^c and \mathbf{b}_2^c are defined such that $\mathbf{a}_i^c \cdot \mathbf{b}_j^c = 2\pi \delta_{ij} \forall i, j = 1, 2$. Then, the number L_N of the BZ hexagons of a commensurate cell enclosed within the BZ of SLG formed by $\{\mathbf{b}_1, \mathbf{b}_2\}$ are

$$L_N = \frac{|(\mathbf{b}_1 \times \mathbf{b}_2) \cdot \hat{\mathbf{z}}|}{|\mathbf{b}_1^c \times \mathbf{b}_2^c \cdot \hat{\mathbf{z}}|} = p_1^2 + p_2^2 + p_1 p_2. \quad (\text{D4})$$

1. Fractal dimension (D_f) in the metric space of p_1, p_2

An irregular hexagon is formed for higher magnitudes of p_1, p_2 along with the smaller hexagons for lower magnitudes. This self-similar, small irregular hexagons lead to the fractality in the metric space (\mathbb{Z}^2 , Euclidean). The fractality in the arrangement of the coefficients p_1, p_2 in this space is shown in Fig. 8. Here we calculate the Hausdorff dimension D_f in the metric space (\mathbb{Z}^2 , Euclidean) of coefficients p_1, p_2 with the Euclidean distance. We calculate the D_f using the

box-counting theorem [1,4]

$$D_f = \lim_{k \rightarrow \infty} \frac{\ln(n_k)}{\ln(2^k)}, \quad (\text{D5})$$

where n_k is number of smaller polygons that completely fit inside a bigger polygon at the k th iteration. There are 3^k small irregular hexagons that fit inside the bigger irregular hexagon at the k th iteration and, therefore, the fractal dimension is then given by

$$D_f = \frac{\ln(3)}{\ln(2)} \sim 1.585.$$

Note that the fractality in this metric space of p_1, p_2 is different from the fractality that we observed in MFs, where D_f is a function of q, p that characterizes a given commensuration, whereas $D_f \sim 1.585$ in the metric space of p_1, p_2 is constant.

APPENDIX E: MORE ON THE INCOMMENSURATION MEASURE

It can be shown that for a generic (q, p) ,

$$\Delta \mathbf{K} = \begin{cases} \frac{2p}{3\gamma} (2\mathbf{b}_1^{(j)} + \mathbf{b}_2^{(j)}) & \text{if } \gcd(p, 3) = 1 \\ \frac{2p}{3\gamma} \mathbf{b}_2^{(j)} & \text{if } \gcd(p, 3) = 3, \end{cases} \quad (\text{E1})$$

where $\gamma = \gcd(3q - p, 3q + p)$ [142]. For $q = 2n + 1$ with $n = 1, 2, 3, \dots$ and $p = 1$, the shift $\Delta \mathbf{K}$ always equals the side length of the hexagon (ℓ) as shown in Fig. 2(a1) of the main text [12]. Further, the moiré lattice vectors coincide with the lattice vectors of the commensurate cell. In this case, we get

$$\frac{A_{\text{FBZ}}^{(j-1)}}{A_{\text{FBZ}}^{(j)}} = L_N \Rightarrow \frac{\Delta A}{A_{\text{FBZ}}^{(j-1)}} = 0. \quad (\text{E2})$$

Similarly, if $q = 2n$ with $n = 1, 2, 3, \dots$ and $p = 1$, the shift $|\Delta \mathbf{K}| = 2\ell$ as shown in Fig. 2(b1) of main text, and the ratio

$$\frac{A_{\text{FBZ}}^{(j-1)}}{A_{\text{FBZ}}^{(j)}} = \frac{4\chi(q) + 1}{4} \Rightarrow \frac{\Delta A}{A_{\text{FBZ}}^{(j-1)}} = \frac{1}{4\chi(q) + 1}, \quad (\text{E3})$$

where $\chi(q)$ is a positive integer dependent on q .

APPENDIX F: THE DETAILS OF THE POTENTIAL, INTERLAYER TUNNELING MATRICES, AND THE BAND STRUCTURES WITH CORRUGATION EFFECTS

The cosine potential that we considered in the main text has a cosine profile, namely,

$$V_j(\mathbf{r}) = V_0 \sum_{i=1}^3 \cos(\mathbf{G}_i^{(j)} \cdot \mathbf{r}), \quad (\text{F1})$$

where $\mathbf{G}_1^{(j)}, \mathbf{G}_2^{(j)}$, and $\mathbf{G}_3^{(j)} = -\mathbf{G}_1^{(j)} - \mathbf{G}_2^{(j)}$ are the reciprocal lattice vectors satisfying $\mathbf{t}_i^{(j)} \cdot \mathbf{G}_k^{(j)} = 2\pi \delta_{ik} \forall i, k = 1, 2$. V_0 is the strength of the potential and the $\mathbf{t}_i^{(j)}$ vectors are defined in the main text.

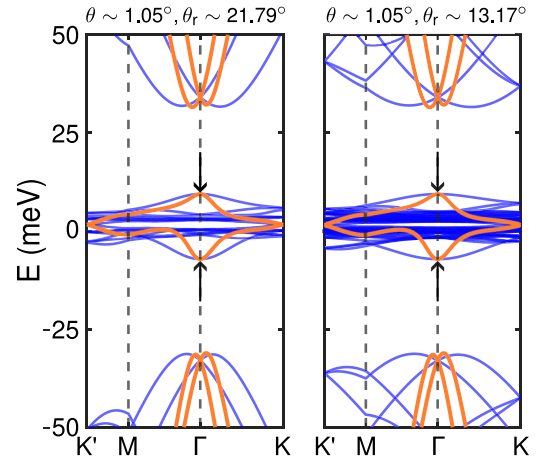


FIG. 9. The inclusion of corrugation effects leads to different interlayer hopping parameters, namely, $t_{\text{AA, BB}} = 79.7$ meV and $t_{\text{AB, BA}} = 97.5$ meV [96]. This does not change the $2e^{2\ln(n_c)/D_f} - 2$ bands inserted within the band gap of the two lowest bands at the Γ point (shown by the two arrows) in the absence of mEP and hence the corrugated TBLG also does not affect the emergence of fractality.

The spatially dependent interlayer tunneling $T(\mathbf{r})$ in the Hamiltonian in Eq. (2) of the main text is given by [11,77,78]

$$\begin{aligned} T(\mathbf{r}) &= \sum_{i=1}^3 T_i e^{-i\mathbf{q}_i \cdot \mathbf{r}} \\ &= \sum_{i=1}^3 \{ \sigma_0 t_{\text{AA, BB}} + [\sigma_x \cos(i-1)\phi \\ &\quad + \sigma_y \sin(i-1)\phi] t_{\text{AB, BA}} \} e^{-i\mathbf{q}_i \cdot \mathbf{r}}, \end{aligned} \quad (\text{F2})$$

where $t_{\text{AA, BB}}$ and $t_{\text{AB, BA}}$ are the interlayer hopping parameters in the local AA/BB regions and AB/BA regions, respectively. σ_0 is a second-order identity matrix and (σ_x, σ_y) are the Pauli matrices. The band structures in Figs. 2 and 4 of the main text are obtained by considering the hopping parameters $t_{\text{AA, BB}} = t_{\text{AB, BA}} = 110$ meV [11] where we ignore the variations in the hopping parameters which occur due to corrugation or atomic relaxations [24] in different regions. The inclusion of this effect leads to different interlayer hopping parameters in both the regions, namely, $t_{\text{AA, BB}} = 79.7$ meV and $t_{\text{AB, BA}} = 97.5$ meV [96]. The band structures with these values of hopping parameters are shown in Fig. 9. The emergent fractality remains unaffected and when the fractal dimension is changed from $D_f = 1.129$ to $D_f = 1.093$ in going from left to right, an identical number $2e^{2\ln(n_c)/D_f} - 2$ of bands are inserted within the band gap of ~ 13 meV at the Γ point.

APPENDIX G: SOME REALISTIC SYSTEMS TO REALIZE THE MODEL HAMILTONIAN (2) OF THE MAIN TEXT AT THE FIRST ITERATION OF THE POTENTIAL

To supplement our assertion in the main text that the MFs introduced through the model Hamiltonian $H_2(\mathbf{r})$ in Eq. (2) of the main text can provide a general description of a number of realistic SMSs, we shall explicitly provide the modeling for three representative SMSs in terms of MFs. For the first

TABLE II. Explicit form of H_{pert} for trilayer and tetralayer graphene systems after ignoring the vector potential term. The quantity \mathcal{I}_2 is the second-order identity matrix and σ_z is z component of the Pauli matrix. $V^S(\mathbf{r})$ in (G3) consists of various moiré potentials V_{ij}^{eff} between the layers. The integer subscripts ij in different terms appear above, referring to the layer indices as indicated in Fig. 11. The detailed expressions for various terms in H_{pert} for each SMS are given in the text.

System	$H_{\text{pert}}(\mathbf{r})$
Trilayer system	$\begin{pmatrix} \hbar^2 v_F^2 M_{11'}^{\text{eff}}(\mathbf{r}) \sigma_z & 0 \\ 0 & \hbar^2 v_F^2 M_{21'}^{\text{eff}}(\mathbf{r}) \sigma_z + \mathcal{I}_2 V_{21'}^{\text{eff}}(\mathbf{r}) - \mathcal{I}_2 V_{11'}^{\text{eff}}(\mathbf{r}) \end{pmatrix}$
Tetralayer system	$\begin{pmatrix} \hbar^2 v_F^2 M_{11'}^{\text{eff}}(\mathbf{r}) \sigma_z + \mathcal{I}_2 V_{12'}^{\text{eff}} & 0 \\ 0 & \mathcal{I}_2 V_{21'}^{\text{eff}}(\mathbf{r}) + \hbar^2 v_F^2 M_{21'}^{\text{eff}}(\mathbf{r}) \sigma_z + \mathcal{I}_2 V_{22'}^{\text{eff}}(\mathbf{r}) + \hbar^2 v_F^2 M_{22'}^{\text{eff}}(\mathbf{r}) \sigma_z - \mathcal{I}_2 V_{11'}^{\text{eff}}(\mathbf{r}) \end{pmatrix}$

iteration $j = 2$ of the mEP, the supermoiré Hamiltonian $H(\mathbf{r})$ can be written as a combination of the Hamiltonian of the MF and a weak periodic perturbation as

$$H(\mathbf{r}) = H_2(\mathbf{r}) + H_{\text{pert}}(\mathbf{r}), \quad (\text{G1})$$

where the periodic perturbation $H_{\text{pert}}(\mathbf{r})$ satisfies

$$H_{\text{pert}}(\mathbf{r} + n_1 \mathbf{a}_1^{(2)} + n_2 \mathbf{a}_2^{(2)}) = H_{\text{pert}}(\mathbf{r}), \quad (\text{G2})$$

where $\mathbf{a}_i^{(2)}$ for $i = 1, 2$ are the primitive lattice vectors of the supermoiré cell as defined in the main text. To do this, let us note that it has already been established [69,70] that for moiré systems such as graphene-graphene or graphene-hBN, the full Hamiltonian can be written as an effective one-layer Hamiltonian experiencing a moiré-periodic potential as

$$V_{\text{moiré}} = V^S(\mathbf{r}) \mathcal{I}_2 + \hbar^2 v_F^2 M^{\text{eff}}(\mathbf{r}) \sigma_z + \hbar v_F e \mathbf{A}^{\text{eff}}(\mathbf{r}) \cdot \boldsymbol{\sigma}. \quad (\text{G3})$$

On the left-hand side (LHS) of Eq. (G3), the strength of each term is of the same order and is directly proportional to the square of the interlayer hopping parameter and can be controlled by the interlayer bias V_{STM} (inversely proportional), which is typically of the order of the bias applied to the tip of the STM that ranges from 20–500 meV [91,92]. $V^S(\mathbf{r})$ preserves the inversion symmetry, the effective mass term $M^{\text{eff}}(\mathbf{r})$ breaks the inversion symmetry while the effective vector potential $\mathbf{A}^{\text{eff}}(\mathbf{r})$ represents a pseudomagnetic field. In the rest of the calculation, we ignore the effective vector potential (G3) since it does not change the proposed insertion of in-gap bands. Thus, the first two terms on the LHS of Eq. (G3) form a H_{pert} whose details for both the tri- and tetralayer supermoiré graphene systems are given in Table II. In the following, we provide the specifics for each SMS.

1. A graphene trilayer system

We consider an AAA-stacked trilayer system [55–57] such that the top graphene layer is at a distance $d = 3d_0 \sim 1$ nm, where d_0 is the interlayer perpendicular distance between the remaining two layers. The configuration is shown in Fig. 11(a), where the top layer is rotated to an angle $3\theta_r/2$, the middle layer is rotated to $\theta_r/2$ while the bottom layer is rotated at an angle $-\theta_r/2$ such that the relative misorientation between any two layers is θ_r . Due to the relatively large distance ($d/d_0 > 1$), the top layer couples only weakly with the remaining two layers. The details of the various terms that appeared in the corresponding Hamiltonian H as had appeared

in (G1) are as follows:

$$H_2(\mathbf{r}) = \begin{pmatrix} h_1(\theta_r/2) + V_{11'}^{\text{eff}}(\mathbf{r}) & T_{12}(\mathbf{r}) \\ T_{12}^\dagger(\mathbf{r}) & h_2(-\theta_r/2) + V_{11'}^{\text{eff}}(\mathbf{r}) \end{pmatrix}. \quad (\text{G4})$$

The integer subscripts ij that appeared in different terms in the Hamiltonian (G4) again refer to the layer indices as indicated in Fig. 11. These terms, as well as the terms that appeared in H_{pert} as shown in Table II have the detailed expression as follows:

$$V_{l1'}^{\text{eff}}(\mathbf{r}) = \frac{6t_{11'}^2}{V_{\text{STM}}} + \frac{t_{11'}^2}{V_{\text{STM}}} \sum_{j=1}^3 \cos(\mathbf{G}_j^{l1'} \cdot \mathbf{r}), \quad (\text{G5a})$$

$$\hbar^2 v_F^2 M_{l1'}^{\text{eff}}(\mathbf{r}) = \frac{\sqrt{3}t_{11'}^2}{V_{\text{STM}}} \sum_{j=1}^3 \sin(\mathbf{G}_j^{l1'} \cdot \mathbf{r}). \quad (\text{G5b})$$

For the moiré reciprocal lattice vector, the superscript l indicates the layers involved and is numbered according to Fig. 11, with $l = 1, 2$. The subscript j numbers such reciprocal lattice vectors between the two surfaces and $\mathbf{G}_3^{l1'} = -\mathbf{G}_1^{l1'} - \mathbf{G}_2^{l1'}$. For $l = 1$, $V_{11'}^{\text{eff}}(\mathbf{r})$ and $\hbar^2 v_F^2 M_{11'}^{\text{eff}}(\mathbf{r})$ are shown in Fig. 12. The hopping parameters are $t_{11'} = t_{AA/BB}(d) = t_{AB/BA}(d) \sim 7.31$ meV, $t_{21'} = t_{AA/BB}(d + d_0) = t_{AB/BA}(d + d_0) \sim 1.41$ meV. As a representative value, for $V_{\text{STM}} = 40$ meV, the strength of the potential becomes $t_{11'}^2/V_{\text{STM}} \sim 1.334$ meV and $t_{21'}^2/V_{\text{STM}} \sim 0.05$ meV.

To proceed further with the calculation, we note that for a commensurate angle θ_r corresponding to q, p in (D2), the

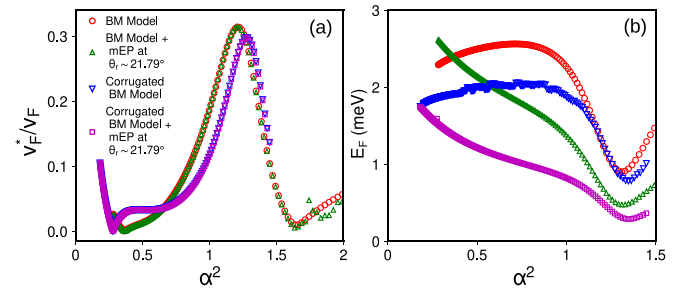


FIG. 10. (a) The renormalized Fermi velocity v_F^*/v_F as a function of α^2 and hence the twist angle θ . (b) The Fermi energy (E_F) as a function of α^2 . Similar to the case of a pristine TBLG [11] or an unrotated mEP to TBLG [83], the renormalized Fermi velocity in the presence of a rotated mEP remains unaffected both in the absence and the presence of the corrugation effect.

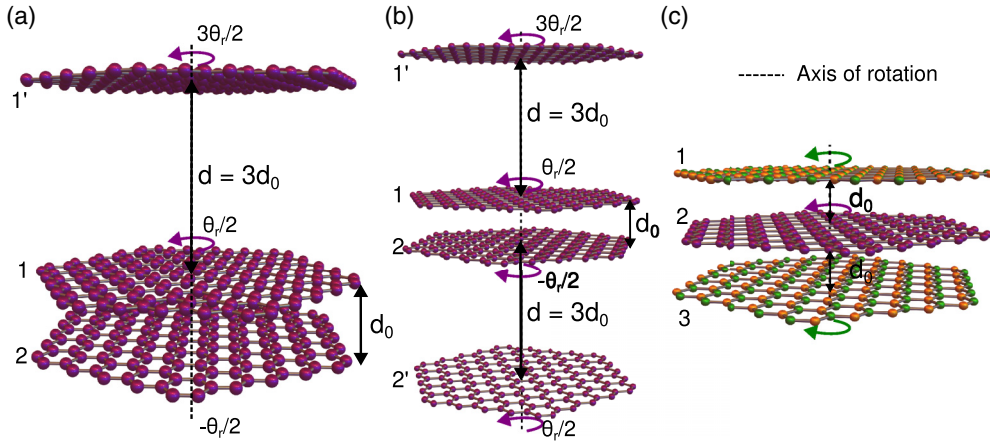


FIG. 11. (a) Trilayer-, (b) four-layer-twisted graphene, and (c) a trilayer boron nitride-graphene-boron nitride system. The above \bullet denote carbon, \bullet boron and \bullet nitrogen atoms, respectively. The angle θ_r is one of the commensurate angles and $d_0 \sim 0.335$ nm is the interlayer separation in TBLG. The number beside each layer represents the layer index used in the text in Appendix H.

two coprime integers for $2\theta_r$ are q', p' that can be obtained from q, p as $p' = 6pq/\text{gcd}(6qp, 3q^2 - p^2)$ and $q' = (3q^2 - p^2)/\text{gcd}(6qp, 3q^2 - p^2)$. After doing straightforward algebra, one can obtain the relation between the reciprocal lattice vectors of two interfaces as

$$\begin{pmatrix} \mathbf{G}_1^{11'} \\ \mathbf{G}_2^{11'} \end{pmatrix} = \begin{pmatrix} Z_1(q, p) & Z_2(q, p) \\ Z_3(q, p) & Z_4(q, p) \end{pmatrix} \begin{pmatrix} \mathbf{G}_1^{21'} \\ \mathbf{G}_2^{21'} \end{pmatrix}, \quad (\text{G6})$$

where Z_1, \dots, Z_4 are integers and are functions of q, p . As an example, for $q = 3$ and $p = 1$, the two coprime integers are obtained as $q' = 13$ and $p' = 9$, yielding $Z_1 = 1, Z_2 = -1, Z_3 = 1$ and $Z_4 = 2$, in (G6). With these, we calculate the first-order correction to the energy eigenvalues of $H_2(\mathbf{r})$ due to $H_{\text{pert}}(\mathbf{r})$. The unperturbed eigenvalues of $H_2(\mathbf{r})$ and the corrected eigenvalues to the first order in perturbation H_{pert} are shown in Fig. 13 for $q = 3$ and $p = 1$ for different values of V_{STM} . From the band structure, we see that the first-order corrections to the energy eigenvalues of $H_2(\mathbf{r})$ become smaller as the interlayer bias V_{STM} increases. Therefore, we can conclude that the number of bands $4e^{2\ln(n_c)/D_f} - 2$ do not change under the effect of the perturbation.

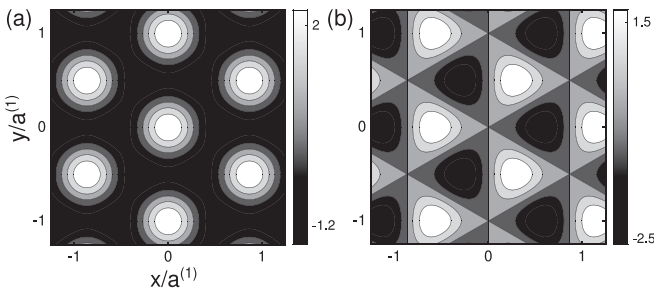


FIG. 12. (a) The spatial variation of the inversion symmetry preserving part $V_{11'}^{\text{eff}}(\mathbf{r})$, where the color bar is in the units of $t_{11'}^2/V_{\text{STM}}$, and (b) the spatial variation of the mass-dependent term $M_{11'}^{\text{eff}}(\mathbf{r})$ that breaks the inversion symmetry. Here, the color bar is in the units of $\sqrt{3}t_{11'}^2/V_{\text{STM}}$.

2. A graphene tetralayer system [87,88]

The second example of the SMS that we consider is where TBLG is sandwiched between two graphene layers, each of which lie at a distance $d = 3d_0$ from it as shown in Fig. 11(b). For this system too, the unperturbed Hamiltonian can be presented as $H_2(\mathbf{r})$ in (G4). For the expression of H_{pert} , we only retain the interlayer coupling between the nearest-neighbor layers which are dominant over the strengths of the interlayer potential in the next-nearest neighbor coupling. Therefore, we ignore $V_{12'}^{\text{eff}}(\mathbf{r})$, $V_{12''}^{\text{eff}}(\mathbf{r})$ and $\hbar^2 v_F^2 M_{21'}^{\text{eff}}(\mathbf{r})$ in the H_{pert} in Table II,

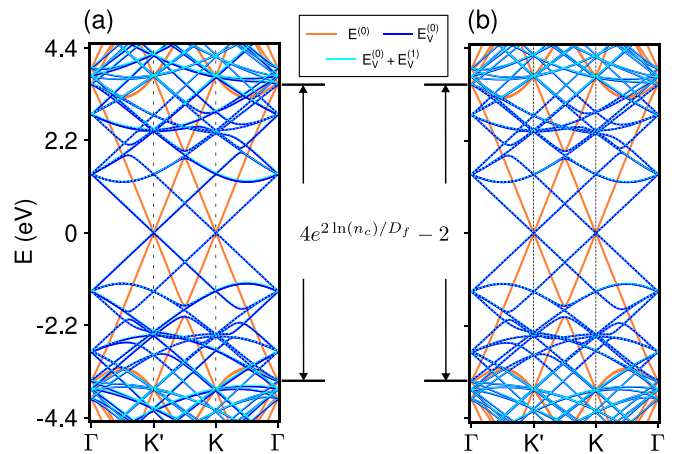


FIG. 13. The band structure corresponding to the trilayer graphene system with increasing values of the interlayer bias voltage (a) $V_{\text{STM}} = 10$ meV and (b) $V_{\text{STM}} = 40$ meV. The solid orange lines show the band structure in the absence of the potential while the blue lines represent the eigenvalues of $H_2(\mathbf{r})$ without the perturbation, while the cyan lines show the band structure of $H_2(\mathbf{r}) + H_{\text{pert}}(\mathbf{r})$ calculated up to the first order in perturbation. The dotted cyan lines show $4e^{2\ln(n_c)/D_f} - 2$ bands within the band gap of lowest two bands at the Γ point.

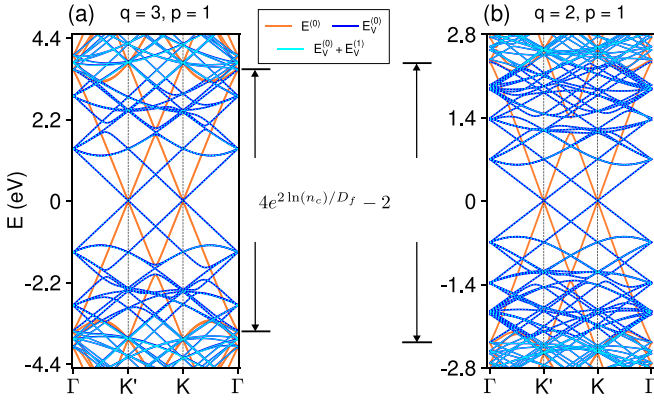


FIG. 14. The band structure of the tetralayer graphene system as shown in Fig. 11(b) for $V_{\text{STM}} = 20$ meV. The solid orange lines show the band structure in the absence of the potential while the blue lines represent the eigenvalues of $H_2(\mathbf{r})$ without the perturbation, while the cyan lines show the band structure of $H_2(\mathbf{r}) + H_{\text{pert}}(\mathbf{r})$ calculated up to the first order in perturbation. The dotted cyan lines show $4e^{2 \ln(n_c)/D_f} - 2$ bands within the band gap of lowest two bands at the Γ point.

and H_{pert} finally becomes

$$H_{\text{pert}}(\mathbf{r}) = \begin{pmatrix} \hbar^2 v_F^2 M_{11'}^{\text{eff}}(\mathbf{r}) \sigma_z & 0 \\ 0 & V_{22'}^{\text{eff}}(\mathbf{r}) + \hbar^2 v_F^2 M_{22'}^{\text{eff}}(\mathbf{r}) \sigma_z - V_{11'}^{\text{eff}}(\mathbf{r}) \end{pmatrix}. \quad (\text{G7})$$

Explicit form of different terms in $H_2(\mathbf{r})$ and $H_{\text{pert}}(\mathbf{r})$ can be written as

$$V_{ll'}^{\text{eff}}(\mathbf{r}) = \frac{6t_{ll'}^2}{V_{\text{STM}}} + \frac{t_{ll'}^2}{V_{\text{STM}}} \sum_{j=1}^3 \cos(\mathbf{G}_j^{ll'} \cdot \mathbf{r}), \quad (\text{G8a})$$

$$\hbar^2 v_F^2 M_{ll'}^{\text{eff}}(\mathbf{r}) = \frac{\sqrt{3}t_{ll'}^2}{V_{\text{STM}}} \sum_{j=1}^3 \sin(\mathbf{G}_j^{ll'} \cdot \mathbf{r}). \quad (\text{G8b})$$

The different superscripts and subscripts used have the same meaning as in the previous case. With the H_{pert} given in (G7), we calculate the first-order correction to the energy eigenvalues. The unperturbed and perturbed band structures to the first order in perturbation theory are shown in Fig. 14 for $q = 3$ and $p = 1$ for comparison. Evidently, the number of bands $4e^{2 \ln(n_c)/D_f} - 2$ do not change under the effect of the perturbation up to the leading order correction.

3. A trilayer system of dissimilar layers

To show that the modeling of a SMS with the Hamiltonian $H_2(\mathbf{r})$ of MF and a periodic perturbation holds beyond merely multilayer graphene systems, we consider a system of dissimilar layers [60] such that a graphene layer is sandwiched between two hBN layers which are a distance d_0 apart as shown in Fig. 11(c). This system can be modeled as a MF at the first iteration of the potential without any perturbing potential, but with a modified $H_2(\mathbf{r})$, namely,

$$H_2(\mathbf{r}) \rightarrow H_2'(\mathbf{r}) = -i\hbar v_F \boldsymbol{\sigma}_{\theta_r/2} \cdot \nabla + V_{21}(\mathbf{r}) + V_{23}(\mathbf{r}), \quad (\text{G9})$$

where $V_{2l}(\mathbf{r})$ is the effective periodic potential due to the hBN layer- $l = 1, 3$ on the graphene layer 2. This is in contrast to examples 1 and 2 above since the Hamiltonian $H_2'(\mathbf{r})$ itself describes the MF at the first iteration and the perturbation is zero. To progress further, we first find the relative misorientation between the hBN and graphene layer, using

$$\theta = \sin^{-1}[(1 + \delta) \sin(\phi)] - \phi, \quad (\text{G10})$$

such that they make a commensurate angles θ_r between them, i.e., we want the difference $|\phi_1 - \phi_2|$ to be one of the commensurate angle $\theta_r(q, p)$, where ϕ is the orientation of the moiré pattern with the graphene layer. Each potential consists of three terms [70], where the different spatially dependent terms are given as

$$V_{2l}^{\text{eff}}(\mathbf{r}) = -3t_0^2 \left(\frac{1}{V_N} + \frac{1}{V_B} \right) - t_0^2 e^{-i\psi} \left(\frac{1}{V_N} + \omega \frac{1}{V_B} \right) \sum_{l=1}^3 \cos \alpha_l^{2l}(\mathbf{r}), \quad (\text{G11a})$$

$$\hbar^2 v_F^2 m_{2l}^{\text{eff}}(\mathbf{r}) = -\sqrt{3}t_0^2 e^{-i\psi} \left(\frac{1}{V_N} + \omega \frac{1}{V_B} \right) \sum_{l=1}^3 \sin \alpha_l^{2l}(\mathbf{r}), \quad (\text{G11b})$$

$$\hbar e v_F A_{2l}^{\text{eff}}(\mathbf{r}) = -2t_0^2 e^{-i\psi} \left(\frac{1}{V_N} + \omega \frac{1}{V_B} \right) \sum_{l=1}^3 \{ \cos[\phi(l+1)] \hat{x} + \sin[\phi(l+1)] \hat{y} \} \cos \alpha_l^{2l}(\mathbf{r}), \quad (\text{G11c})$$

where $t_0 = 0.152$ eV, $\omega = e^{i2\pi/3}$, $\psi \sim -0.29$ rad, $V_N = 3.34$ eV and $V_B = -1.4$ eV for boron and nitride atoms [73], and

$$\alpha_l^{2l} = \mathbf{G}_l^{2l} \cdot \mathbf{r} + \psi + 2\pi/3. \quad (\text{G12})$$

For three different values of q, p and hence the θ_r , the band structures along the high symmetry path X-Y-K-X are shown in Fig 15. It may be noted that in the band structure plot we have chosen the path through the high-symmetry points differently as compared to the one used in the preceding two examples of supermoiré structures consisting only out of graphene layers. This is in accordance with the convention used in [73]. The high-symmetry point Y encloses $2e^{2 \ln n_c/D_f} - 1$ in-gap bands within the band gap of the lowest two bands shown by the double-headed arrow. This example of dissimilar layers also exhibits the robustness of the insertion of a controlled number of bands determined by the fractal dimension D_f of the MF. Therefore, the MF can also explain the band structure of such a system.

APPENDIX H: DISCUSSION ON THE PROBABILITY-DENSITY PLOT FOR THE MOIRÉ-FRACTAL WAVE FUNCTIONS GIVEN IN FIGS. 2 AND 4 OF THE MAIN TEXT

The probability density corresponding to the wave functions of the MF at the first iteration $j = 2$ for the Hamiltonian (2) of the main text were plotted in Figs. 2(a4) and 2(b4)

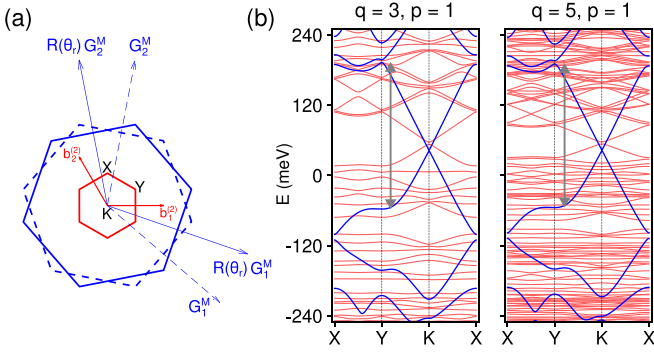


FIG. 15. (a) The two blue and dashed blue hexagons show the moiré BZ of the top and bottom moiré interfaces for the trilayer hBN-hBN shown in Fig. 11(c). The inner red hexagon is the super-moiré BZ. (b) The band structures for two different values of q, p along the high-symmetry path X - Y - K - X [73] as shown in (b). The solid blue lines show the band structures of the graphene-hBN system with $V_2(\mathbf{r}) = 0$ while the solid red lines represent graphene sandwiched between two hBN layers as in Fig. 11(c). The two dark-gray arrows show the band gap between two lowest bands at the Y point where the $2e^{2\ln(n_c)/D_f} - 1$ bands are inserted.

and also in the third column of Fig. 4 in the main text. To that purpose, we have calculated the spatial variation of the probability density $\rho_{nk}(\mathbf{r}) = |\psi_{nk}(\mathbf{r})|^2$ of the Bloch states, where n is the band index and \mathbf{k} is the Bloch wave vector. Specifically, we calculated $\rho_{nk}(\mathbf{r})$ corresponding to the conduction band at the Dirac point over the area in real space covering the first supermoiré-cell. $\theta = \theta_r(3, 1) \sim 21.79^\circ$ and $\theta_r(2, 1) \sim 32.20^\circ$, the $\rho_K(\theta)$ is shown in the Figs. 2(a4) and 2(b4) of the main text and $\theta \sim 1.05^\circ$ and $\theta_r(3, 1) \sim 21.79^\circ$ is shown in Fig. 4(a) and for $\theta \sim 1.05^\circ$ and $\theta_r(5, 1) \sim 13.17^\circ$ in Fig. 4(b).

For both plots, the WS unit cell is shown with solid black lines (see Figs. 2 and 4) that encloses $2e^{2\ln(n_c)/D_f}$ local maxima or minima of $\rho_{c(v)K}(\mathbf{r})$. We numerically verified that this happens for both the high-symmetry K and M points, while the number of maxima or minima enclosed by the WS cell at the Γ point is different.

APPENDIX I: CALCULATION OF THE HUBBARD PARAMETERS

The Hubbard interaction U_H can be written as [143]

$$U_{R'm', Rm} = \sum_{XX'} \int d\mathbf{r}' d\mathbf{r} |\phi_{m'}^{X'}(\mathbf{r}', \mathbf{R}')|^2 U_C(\mathbf{r}', \mathbf{r}) |\phi_m^X(\mathbf{r}, \mathbf{R})|^2, \quad (\text{I1})$$

where $U_C(\mathbf{r}', \mathbf{r})$ is the screened Coulomb interaction and $\phi_m^X(\mathbf{r}, \mathbf{R})$ is the Wannier orbital of the sublattice X and band index m that is centered at the \mathbf{R} th lattice site. For pristine TBLG, the localized Wannier orbitals can be constructed from the Bloch states of the Hamiltonian H_1 in Eq. (2) of the main text corresponding to the two flat bands near the Fermi level and these orbitals are centered at the local AB/BA regions of the moiré pattern [96, 144, 145]. Following this prescription

[145], for the on-site Hubbard interaction U_0 one can write

$$U_0 \propto \frac{e^2}{a^{(1)}}, \quad (\text{I2})$$

where e is the electronic charge and the moiré wavelength $a^{(1)}$ provides the cutoff for the screening. In the MF model due to the presence of the mEP in H_j for $j \geq 2$ in Eq. (2) of the main text, the Bloch states $\psi_{nk}^{(j)}(\mathbf{r})$ corresponding to the j th iteration of the potential have the Bloch periodicity corresponding to the moiré supercell that can be expressed as

$$\psi_{nk}^{(j)}(\mathbf{r} + \mathbf{a}^{(j)}) = e^{i\mathbf{k} \cdot \mathbf{a}^{(j)}} \psi_{nk}^{(j)}(\mathbf{r}). \quad (\text{I3})$$

The translational-invariant Wannier functions, made out of superposing these Bloch states, will be centered at the lattice sites given by $\mathbf{a}^{(j)}$. Accordingly, the on-site Hubbard interaction U_0 that has the lattice constant as a cutoff length will be scaled. However it may be mentioned that the Wannier orbitals are constructed through self-consistent *ab initio* calculations and depend upon the number of chosen bands [144–146]. In a MF, $2e^{2\ln(n_c/D_f)} - 2$ inner bands can be considered, since they are well separated from the other higher bands (see Fig. 4 in main text and Fig. 5 here). A more detailed calculation may lead to a more precise quantitative estimate of U_0 in the MF, but this is beyond the scope of the current paper. Nevertheless, following the above argument, we can estimate the on-site Hubbard interaction for the j th iteration of the potential as

$$U_0^{(j)} \propto \frac{e^2}{\epsilon a^{(j)}}. \quad (\text{I4})$$

If U_0 is the on-site Hubbard interaction for pristine TBLG, then for $j = 2$, it becomes $U_0 \rightarrow U_0/s$, where s is the contractivity factor as defined in the main text. Particularly, for $q = 3$ and $p = 1$, the contractivity factor $s = \sqrt{7}$. For the bandwidth t_w , however, we do not have any such simple scaling argument. The bandwidth $t_w = \max(E_n) - \min(E_n)$, where E_n is the energy of the n th band, can be determined as a function of the strength of the potential V_0 . Hence we determine this numerically and present the results in Figs. 16(a) and 16(b). It can be seen that that the bandwidth depends on both V_0 as well as the hopping parameters. Even though the bandwidth gets significantly reduced as compared to pristine TBLG, the full behavior is not amenable to simple explanation. As an example, $t_w/t_{w0} \sim 0.04$ for the conduction band at $V_0 = 1.2$ meV as shown in Fig. 16(a) for $t_{AA/BB} = t_{AB/BA} = 110$ meV [11]. Therefore, the Hubbard ratio U/t_w becomes $1/(\sqrt{7} \times 0.04) \sim 9.4$ of the ratio of pristine TBLG.

APPENDIX J: MORE ON THE EXPERIMENTAL SIGNATURES OF MOIRÉ FRACTALS

In the presence of the first iteration of an external potential $V_2(\mathbf{r})$, the in-gap bands near the Fermi surface, situated within the energy window of the lowest two bands, contribute to a greater number of dips and peaks in the density of states (refer to Figs. 2 and 4 of the main text). This effect arises from the curvature of these additional bands, resulting in changes to the density of states within that energy range. Since the differential conductance (dI/dV) in the various real-space probes is proportional to the DOS of the sample at a particular

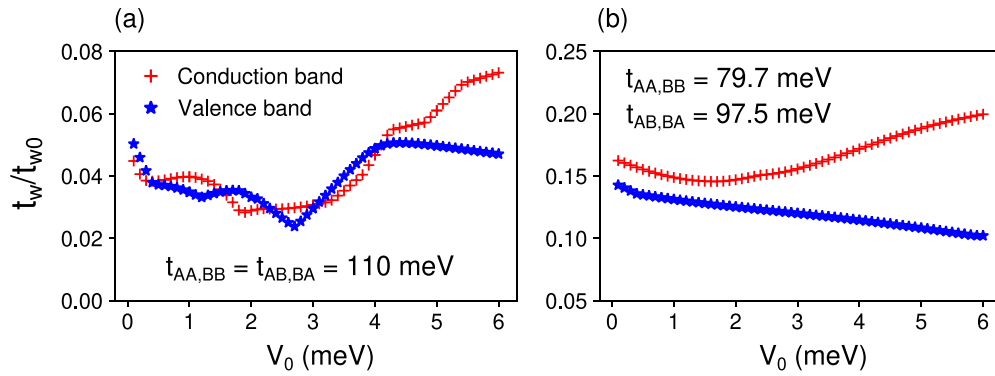


FIG. 16. The bandwidth of the conduction and valence band in the presence of mEP for $q = 3$, $p = 1$ for (a) $t_{AA, BB} = t_{AB, BA} = 110$ meV [11], (b) $t_{AA, BB} = 79.7$ meV, and $t_{AB, BA} = 97.5$ meV [24,96]. The bandwidth t_w is in the unit of t_{w0} , which is the bandwidth of pristine TBLG at $\theta \sim 1.05^\circ$.

bias voltage V_{bias} [147],

$$dI/dV \propto \rho_{\text{sample}}(-e V_{\text{bias}}), \quad (\text{J1})$$

where e is the fundamental electron charge. The increased DOS of the sample leads to an increased conductance within a given energy window. In the case of the quantum twisting microscope [94], which offers better real-space probing due to the local interference at the tip, the increased number of states at a particular location \mathbf{r} may lead to an enhanced coupling among these states and therefore alter the transport properties in contrast to the case when there is no such external potential.

The calculation of experimentally measurable optical properties involves the calculation of the optical matrix elements between the Bloch states of different (same) band indices, i.e., the interband (intra-band) transitions [43,130,131]. Due to the greater number of states available within a given energy window, there may be nonvanishing optical matrix elements between the induced in-gap states that can further tune those properties and, therefore, optical measurements also provide a technique for characterizing MFs.

A recent article [132] reported cryogenic near-field optoelectronic measurements of hBN-encapsulated MATBLG where the photovoltage measurements revealed a supermoiré pattern whose periodicity was embedded in the photovoltage response. In their experiment, the top graphene layer was aligned with the top encapsulating hBN layer, while the bottom graphene layer was twisted by an angle θ_{hBN} with respect to the hBN layer, and the two graphene layers were relatively twisted by $\theta_{\text{TB LG}}$. Since the Moiré wavelength for the graphene-hBN interface is limited to ~ 14 nm due to the lattice mismatch of 1.8%, there is a finite mismatch in the moiré wavelengths of both the graphene-hBN and the graphene-graphene interfaces at smaller angles. For MFs in hBN-encapsulated graphene (Fig. 15), both the hBN layers with respect to the graphene layer are rotated to the same angle, thereby enabling the same moiré wavelengths in both the graphene-hBN interfaces. Thus, for the two cases with $(q, p) = (3, 1)$ and $(q, p) = (5, 1)$, the supermoiré wavelengths become $\lambda_{\text{SM}} \sim 36.13$ nm and $\lambda_{\text{SM}} \sim 60.24$ nm, respectively. A similar photovoltage response measurement in hBN-encapsulated graphene may also show supermoiré signatures.

-
- [1] B. B. Mandelbrot, *The Fractal Geometry of Nature* (W.H. Freeman, New York, 1983).
- [2] J. Feder, *Fractals*, Physics of Solids and Liquids (Plenum Press, New York, 1988).
- [3] P. F. Duvall and L. S. Husch, *Proc. Am. Math. Soc.* **116**, 279 (1992).
- [4] H. Lauwerier and H. Lauwerier, *Fractals: Endlessly Repeated Geometrical Figures* (Penguin Books, London, 1991).
- [5] M. F. Dacey, *J. Reg. Sci.* **5**, 63 (1964).
- [6] J. Malczewski, in *International Encyclopedia of Human Geography*, edited by R. Kitchin and N. Thrift (Elsevier, Oxford, 2009), pp. 26–30.
- [7] J. M. B. Lopes dos Santos, N. M. R. Peres, and A. H. Castro Neto, *Phys. Rev. Lett.* **99**, 256802 (2007).
- [8] E. Suárez Morell, J. D. Correa, P. Vargas, M. Pacheco, and Z. Barticevic, *Phys. Rev. B* **82**, 121407(R) (2010).
- [9] G. Li, A. Luican, J. M. B. Lopes dos Santos, A. H. Castro Neto, A. Reina, J. Kong, and E. Y. Andrei, *Nat. Phys.* **6**, 109 (2010).
- [10] J. Hicks, M. Sprinkle, K. Shepperd, F. Wang, A. Tejada, A. Taleb-Ibrahimi, F. Bertran, P. Le Fèvre, W. A. de Heer, C. Berger, and E. H. Conrad, *Phys. Rev. B* **83**, 205403 (2011).
- [11] R. Bistritzer and A. H. MacDonald, *Proc. Natl. Acad. Sci.* **108**, 12233 (2011).
- [12] J. M. B. Lopes dos Santos, N. M. R. Peres, and A. H. Castro Neto, *Phys. Rev. B* **86**, 155449 (2012).
- [13] C.-C. Lu, Y.-C. Lin, Z. Liu, C.-H. Yeh, K. Suenaga, and P.-W. Chiu, *ACS Nano* **7**, 2587 (2013).
- [14] P. Moon and M. Koshino, *Phys. Rev. B* **87**, 205404 (2013).
- [15] A. O. Sboychakov, A. L. Rakhmanov, A. V. Rozhkov, and F. Nori, *Phys. Rev. B* **92**, 075402 (2015).
- [16] S. Dai, Y. Xiang, and D. J. Srolovitz, *Nano Lett.* **16**, 5923 (2016).

- [17] Y. Cao, J. Y. Luo, V. Fatemi, S. Fang, J. D. Sanchez-Yamagishi, K. Watanabe, T. Taniguchi, E. Kaxiras, and P. Jarillo-Herrero, *Phys. Rev. Lett.* **117**, 116804 (2016).
- [18] M. Andelković, L. Covaci, and F. M. Peeters, *Phys. Rev. Mater.* **2**, 034004 (2018).
- [19] L. Huder, A. Artaud, T. Le Quang, G. T. de Laissardière, A. G. M. Jansen, G. Lapertot, C. Chapelier, and V. T. Renard, *Phys. Rev. Lett.* **120**, 156405 (2018).
- [20] J.-B. Qiao, L.-J. Yin, and L. He, *Phys. Rev. B* **98**, 235402 (2018).
- [21] L. Zou, H. C. Po, A. Vishwanath, and T. Senthil, *Phys. Rev. B* **98**, 085435 (2018).
- [22] Y. Cao, V. Fatemi, S. Fang, K. Watanabe, T. Taniguchi, E. Kaxiras, and P. Jarillo-Herrero, *Nature (London)* **556**, 43 (2018).
- [23] Y. Cao, V. Fatemi, A. Demir, S. Fang, S. L. Tomarken, J. Y. Luo, J. D. Sanchez-Yamagishi, K. Watanabe, T. Taniguchi, E. Kaxiras, R. C. Ashoori, and P. Jarillo-Herrero, *Nature (London)* **556**, 80 (2018).
- [24] S. Carr, D. Massatt, S. B. Torrisi, P. Cazeaux, M. Luskin, and E. Kaxiras, *Phys. Rev. B* **98**, 224102 (2018).
- [25] C. Kumar, S. K. Srivastav, P. Adhikary, S. Banerjee, T. Das, and A. Das, *Phys. Rev. B* **98**, 155408 (2018).
- [26] B. Lian, Z. Wang, and B. A. Bernevig, *Phys. Rev. Lett.* **122**, 257002 (2019).
- [27] S. L. Tomarken, Y. Cao, A. Demir, K. Watanabe, T. Taniguchi, P. Jarillo-Herrero, and R. C. Ashoori, *Phys. Rev. Lett.* **123**, 046601 (2019).
- [28] S. Carr, S. Fang, Z. Zhu, and E. Kaxiras, *Phys. Rev. Res.* **1**, 013001 (2019).
- [29] T. M. R. Wolf, J. L. Lado, G. Blatter, and O. Zilberberg, *Phys. Rev. Lett.* **123**, 096802 (2019).
- [30] K. Yu, N. Van Luan, T. Kim, J. Jeon, J. Kim, P. Moon, Y. H. Lee, and E. J. Choi, *Phys. Rev. B* **99**, 241405(R) (2019).
- [31] E. Y. Andrei and A. H. MacDonald, *Nat. Mater.* **19**, 1265 (2020).
- [32] L. Balents, C. R. Dean, D. K. Efetov, and A. F. Young, *Nat. Phys.* **16**, 725 (2020).
- [33] U. Zondiner, A. Rozen, D. Rodan-Legrain, Y. Cao, R. Queiroz, T. Taniguchi, K. Watanabe, Y. Oreg, F. von Oppen, A. Stern, E. Berg, P. Jarillo-Herrero, and S. Ilani, *Nature (London)* **582**, 203 (2020).
- [34] B. A. Bernevig, Z.-D. Song, N. Regnault, and B. Lian, *Phys. Rev. B* **103**, 205411 (2021).
- [35] Z.-D. Song, B. Lian, N. Regnault, and B. A. Bernevig, *Phys. Rev. B* **103**, 205412 (2021).
- [36] T. Li, S. Jiang, L. Li, Y. Zhang, K. Kang, J. Zhu, K. Watanabe, T. Taniguchi, D. Chowdhury, L. Fu, J. Shan, and K. F. Mak, *Nature (London)* **597**, 350 (2021).
- [37] L. Ma, P. X. Nguyen, Z. Wang, Y. Zeng, K. Watanabe, T. Taniguchi, A. H. MacDonald, K. F. Mak, and J. Shan, *Nature (London)* **598**, 585 (2021).
- [38] R. Debnath, S. Sett, R. Biswas, V. Raghunathan, and A. Ghosh, *Nanotechnology* **32**, 455705 (2021).
- [39] S. M. Gardezi, H. Pirie, S. Carr, W. Dorrell, and J. E. Hoffman, *2D Mater.* **8**, 031002 (2021).
- [40] T. M. R. Wolf, O. Zilberberg, G. Blatter, and J. L. Lado, *Phys. Rev. Lett.* **126**, 056803 (2021).
- [41] N. C. H. Hesp, I. Torre, D. Rodan-Legrain, P. Novelli, Y. Cao, S. Carr, S. Fang, P. Stepanov, D. Barcons-Ruiz, H. Herzig Sheinfux, K. Watanabe, T. Taniguchi, D. K. Efetov, E. Kaxiras, P. Jarillo-Herrero, M. Polini, and F. H. L. Koppens, *Nat. Phys.* **17**, 1162 (2021).
- [42] D. Aggarwal, R. Narula, and S. Ghosh, *J. Phys.: Condens. Matter* **35**, 143001 (2023).
- [43] D. Arora, D. Aggarwal, S. Ghosh, and R. Narula, *Phys. Rev. B* **107**, 205423 (2023).
- [44] W. Christaller and C. Baskin, *Central Places in Southern Germany*, Central Places in Southern Germany (Prentice-Hall, New Jersey, 1966), Vol. 10.
- [45] A. Getis and J. Getis, *J. Geogr.* **65**, 220 (1966).
- [46] R. Hottes, *Ann. Assoc. Am. Geogr.* **73**, 51 (1983).
- [47] A. Lösch and W. Woglom, *The Economics of Location* (Yale University Press, New Haven, 1954).
- [48] J. U. Marshall, *Geogr. Anal.* **7**, 421 (1975).
- [49] A. Cardillo, S. Scellato, V. Latora, and S. Porta, *Phys. Rev. E* **73**, 066107 (2006).
- [50] T. Courtat, C. Gloaguen, and S. Douady, *Phys. Rev. E* **83**, 036106 (2011).
- [51] M. Barthélemy and A. Flammini, *Phys. Rev. Lett.* **100**, 138702 (2008).
- [52] M. Barthélemy, P. Bordin, H. Berestycki, and M. Gribaudi, *Sci. Rep.* **3**, 2153 (2013).
- [53] M. Barthélemy, *Nat. Rev. Phys.* **1**, 406 (2019).
- [54] H. Zhang, T. Lan, and Z. Li, *Int. J. Geogr. Inf. Sci.* **36**, 1100 (2022).
- [55] C. Mora, N. Regnault, and B. A. Bernevig, *Phys. Rev. Lett.* **123**, 026402 (2019).
- [56] Z. Zhu, S. Carr, D. Massatt, M. Luskin, and E. Kaxiras, *Phys. Rev. Lett.* **125**, 116404 (2020).
- [57] A. Uri, S. C. de la Barrera, M. T. Randeria, D. Rodan-Legrain, T. Devakul, P. J. D. Crowley, N. Paul, K. Watanabe, T. Taniguchi, R. Lifshitz, L. Fu, R. C. Ashoori, and P. Jarillo-Herrero, *Nature (London)* **620**, 762 (2023).
- [58] J. Liu, Z. Ma, J. Gao, and X. Dai, *Phys. Rev. X* **9**, 031021 (2019).
- [59] B. Xie, R. Peng, S. Zhang, and J. Liu, *npj Comput. Mater.* **8**, 110 (2022).
- [60] M. Andelković, S. P. Milovanović, L. Covaci, and F. M. Peeters, *Nano Lett.* **20**, 979 (2020).
- [61] D. R. Hofstadter, *Phys. Rev. B* **14**, 2239 (1976).
- [62] C. Albrecht, J. H. Smet, K. von Klitzing, D. Weiss, V. Umansky, and H. Schweizer, *Phys. Rev. Lett.* **86**, 147 (2001).
- [63] D. J. Thouless, M. Kohmoto, M. P. Nightingale, and M. den Nijs, *Phys. Rev. Lett.* **49**, 405 (1982).
- [64] M. Kohmoto, *Ann. Phys.* **160**, 343 (1985).
- [65] K. S. Novoselov, A. K. Geim, S. V. Morozov, D. Jiang, Y. Zhang, S. V. Dubonos, I. V. Grigorieva, and A. A. Firsov, *Science* **306**, 666 (2004).
- [66] K. S. Novoselov, D. Jiang, F. Schedin, T. J. Booth, V. V. Khotkevich, S. V. Morozov, and A. K. Geim, *Proc. Natl. Acad. Sci.* **102**, 10451 (2005).
- [67] A. K. Geim and I. V. Grigorieva, *Nature (London)* **499**, 419 (2013).
- [68] C. Dean, A. Young, L. Wang, I. Meric, G.-H. Lee, K. Watanabe, T. Taniguchi, K. Shepard, P. Kim, and J. Hone, *Solid State Commun.* **152**, 1275 (2012), Exploring Graphene, Recent Research Advances.
- [69] M. Kindermann and P. N. First, *Phys. Rev. B* **83**, 045425 (2011).

- [70] M. Kindermann, B. Uchoa, and D. L. Miller, *Phys. Rev. B* **86**, 115415 (2012).
- [71] J. R. Wallbank, A. A. Patel, M. Mucha-Kruczyński, A. K. Geim, and V. I. Fal'ko, *Phys. Rev. B* **87**, 245408 (2013).
- [72] M. Yankowitz, J. Xue, D. Cormode, J. D. Sanchez-Yamagishi, K. Watanabe, T. Taniguchi, P. Jarillo-Herrero, P. Jacquod, and B. J. LeRoy, *Nat. Phys.* **8**, 382 (2012).
- [73] P. Moon and M. Koshino, *Phys. Rev. B* **90**, 155406 (2014).
- [74] A. H. Castro Neto, F. Guinea, N. M. R. Peres, K. S. Novoselov, and A. K. Geim, *Rev. Mod. Phys.* **81**, 109 (2009).
- [75] S. Reich, J. Maultzsch, C. Thomsen, and P. Ordejón, *Phys. Rev. B* **66**, 035412 (2002).
- [76] R. Bistritzer and A. H. MacDonald, *Phys. Rev. B* **81**, 245412 (2010).
- [77] G. Tarnopolsky, A. J. Kruchkov, and A. Vishwanath, *Phys. Rev. Lett.* **122**, 106405 (2019).
- [78] P. J. Ledwith, E. Khalaf, and A. Vishwanath, *Ann. Phys.* **435**, 168646 (2021), special issue on Philip W. Anderson.
- [79] S. Shallcross, S. Sharma, E. Kandelaki, and O. A. Pankratov, *Phys. Rev. B* **81**, 165105 (2010).
- [80] F. Guinea and N. R. Walet, *Proc. Natl. Acad. Sci.* **115**, 13174 (2018).
- [81] L. Rademaker, D. A. Abanin, and P. Mellado, *Phys. Rev. B* **100**, 205114 (2019).
- [82] Z. A. H. Goodwin, V. Vitale, X. Liang, A. A. Mostofi, and J. Lischner, *Electron. Struct.* **2**, 034001 (2020).
- [83] J. Cao, F. Qi, H. Yang, and G. Jin, *Phys. Rev. B* **103**, 165417 (2021).
- [84] S. Chen, M. He, Y.-H. Zhang, V. Hsieh, Z. Fei, K. Watanabe, T. Taniguchi, D. H. Cobden, X. Xu, C. R. Dean, and M. Yankowitz, *Nat. Phys.* **17**, 374 (2021).
- [85] M. He, Y.-H. Zhang, Y. Li, Z. Fei, K. Watanabe, T. Taniguchi, X. Xu, and M. Yankowitz, *Nat. Commun.* **12**, 4727 (2021).
- [86] S. Xu, M. M. Al Ezzi, N. Balakrishnan, A. Garcia-Ruiz, B. Tsim, C. Mullan, J. Barrier, N. Xin, B. A. Piot, T. Taniguchi, K. Watanabe, A. Carvalho, A. Mishchenko, A. K. Geim, V. I. Fal'ko, S. Adam, A. H. C. Neto, K. S. Novoselov, and Y. Shi, *Nat. Phys.* **17**, 619 (2021).
- [87] G. W. Burg, E. Khalaf, Y. Wang, K. Watanabe, T. Taniguchi, and E. Tutuc, *Nat. Mater.* **21**, 884 (2022).
- [88] Y. Zhang, R. Polski, C. Lewandowski, A. Thomson, Y. Peng, Y. Choi, H. Kim, K. Watanabe, T. Taniguchi, J. Alicea, F. von Oppen, G. Refael, and S. Nadj-Perge, *Science* **377**, 1538 (2022).
- [89] N. R. Finney, M. Yankowitz, L. Muraleetharan, K. Watanabe, T. Taniguchi, C. R. Dean, and J. Hone, *Nat. Nanotechnol.* **14**, 1029 (2019).
- [90] A. Garcia-Ruiz, H.-Y. Deng, V. V. Enaldiev, and V. I. Fal'ko, *Phys. Rev. B* **104**, 085402 (2021).
- [91] Y. Choi, J. Kemmer, Y. Peng, A. Thomson, H. Arora, R. Polski, Y. Zhang, H. Ren, J. Alicea, G. Refael, F. von Oppen, K. Watanabe, T. Taniguchi, and S. Nadj-Perge, *Nat. Phys.* **15**, 1174 (2019).
- [92] K. P. Nuckolls, R. L. Lee, M. Oh, D. Wong, T. Soejima, J. P. Hong, D. Călugăru, J. Herzog-Arbeitman, B. A. Bernevig, K. Watanabe, T. Taniguchi, N. Regnault, M. P. Zaletel, and A. Yazdani, *Nature (London)* **620**, 525 (2023).
- [93] S. L. Arlinghaus, *Geografiska Annaler: Series B, Human Geogr.* **67**, 83 (1985).
- [94] A. Inbar, J. Birkbeck, J. Xiao, T. Taniguchi, K. Watanabe, B. Yan, Y. Oreg, A. Stern, E. Berg, and S. Ilani, *Nature (London)* **614**, 682 (2023).
- [95] M. Barnsley, *Fractals Everywhere*, Dover Books on Mathematics (Dover Publications, Mineola, New York, 2012).
- [96] M. Koshino, N. F. Q. Yuan, T. Koretsune, M. Ochi, K. Kuroki, and L. Fu, *Phys. Rev. X* **8**, 031087 (2018).
- [97] C.-H. Park, L. Yang, Y.-W. Son, M. L. Cohen, and S. G. Louie, *Nat. Phys.* **4**, 213 (2008).
- [98] A. H. MacDonald, *Phys. Rev. B* **28**, 6713 (1983).
- [99] A. H. MacDonald, *Phys. Rev. B* **29**, 3057 (1984).
- [100] In HB problem, $\hat{T}_{a_1}\hat{T}_{a_2} \neq \hat{T}_{a_2}\hat{T}_{a_1}$, where a_1 and a_2 are the direct-lattice PV. To ensure commutativity, magnetic TOs are redefined for the enlarged magnetic unit cell. Dimensionless quantity $\Phi/\Phi_0 = |\mathbf{a}_1 \times \mathbf{a}_2|/l_B^2$ serves as an incommensurability measure with magnetic flux per plaquette Φ , flux quanta $\Phi_0 = \hbar/e$, and magnetic length l_B in the presence of a magnetic field breaking time reversal symmetry.
- [101] M. Koshino and P. Moon, *J. Phys. Soc. Jpn.* **84**, 121001 (2015).
- [102] P. San-Jose and E. Prada, *Phys. Rev. B* **88**, 121408(R) (2013).
- [103] D. K. Efimkin and A. H. MacDonald, *Phys. Rev. B* **98**, 035404 (2018).
- [104] S. G. Xu, A. I. Berdyugin, P. Kumaravadivel, F. Guinea, R. Krishna Kumar, D. A. Bandurin, S. V. Morozov, W. Kuang, B. Tsim, S. Liu, J. H. Edgar, I. V. Grigorieva, V. I. Fal'ko, M. Kim, and A. K. Geim, *Nat. Commun.* **10**, 4008 (2019).
- [105] Z. Wang, Y. B. Wang, J. Yin, E. Tóvári, Y. Yang, L. Lin, M. Holwill, J. Birkbeck, D. J. Perello, S. Xu, J. Zultak, R. V. Gorbachev, A. V. Kretinin, T. Taniguchi, K. Watanabe, S. V. Morozov, M. Anđelković, S. P. Milovanović, L. Covaci, F. M. Peeters *et al.*, *Sci. Adv.* **5**, eaay8897 (2019).
- [106] K. Uchida, S. Furuya, J.-I. Iwata, and A. Oshiyama, *Phys. Rev. B* **90**, 155451 (2014).
- [107] N. N. T. Nam and M. Koshino, *Phys. Rev. B* **96**, 075311 (2017).
- [108] X. Lu, P. Stepanov, W. Yang, M. Xie, M. A. Aamir, I. Das, C. Urgell, K. Watanabe, T. Taniguchi, G. Zhang, A. Bachtold, A. H. MacDonald, and D. K. Efetov, *Nature (London)* **574**, 653 (2019).
- [109] M. Serlin, C. L. Tschirhart, H. Polshyn, Y. Zhang, J. Zhu, K. Watanabe, T. Taniguchi, L. Balents, and A. F. Young, *Science* **367**, 900 (2020).
- [110] K. P. Nuckolls, M. Oh, D. Wong, B. Lian, K. Watanabe, T. Taniguchi, B. A. Bernevig, and A. Yazdani, *Nature (London)* **588**, 610 (2020).
- [111] S. Wu, Z. Zhang, K. Watanabe, T. Taniguchi, and E. Y. Andrei, *Nat. Mater.* **20**, 488 (2021).
- [112] Y. Saito, J. Ge, L. Rademaker, K. Watanabe, T. Taniguchi, D. A. Abanin, and A. F. Young, *Nat. Phys.* **17**, 478 (2021).
- [113] I. Das, X. Lu, J. Herzog-Arbeitman, Z.-D. Song, K. Watanabe, T. Taniguchi, B. A. Bernevig, and D. K. Efetov, *Nat. Phys.* **17**, 710 (2021).
- [114] P. J. Ledwith, G. Tarnopolsky, E. Khalaf, and A. Vishwanath, *Phys. Rev. Res.* **2**, 023237 (2020).
- [115] Y. Cao, D. Rodan-Legrain, J. M. Park, N. F. Q. Yuan, K. Watanabe, T. Taniguchi, R. M. Fernandes, L. Fu, and P. Jarillo-Herrero, *Science* **372**, 264 (2021).
- [116] N. Lecante, S. Javvaji, J. An, A. Samudrala, and J. Jung, *Phys. Rev. B* **106**, 115410 (2022).

- [117] G. W. Burg, J. Zhu, T. Taniguchi, K. Watanabe, A. H. MacDonald, and E. Tutuc, *Phys. Rev. Lett.* **123**, 197702 (2019).
- [118] C. Shen, Y. Chu, Q. Wu, N. Li, S. Wang, Y. Zhao, J. Tang, J. Liu, J. Tian, K. Watanabe, T. Taniguchi, R. Yang, Z. Y. Meng, D. Shi, O. V. Yazyev, and G. Zhang, *Nat. Phys.* **16**, 520 (2020).
- [119] M. He, Y. Li, J. Cai, Y. Liu, K. Watanabe, T. Taniguchi, X. Xu, and M. Yankowitz, *Nat. Phys.* **17**, 26 (2021).
- [120] J. M. Park, Y. Cao, L.-Q. Xia, S. Sun, K. Watanabe, T. Taniguchi, and P. Jarillo-Herrero, *Nat. Mater.* **21**, 877 (2022).
- [121] C. Mullan, S. Slizovskiy, J. Yin, Z. Wang, Q. Yang, S. Xu, Y. Yang, B. A. Piot, S. Hu, T. Taniguchi, K. Watanabe, K. S. Novoselov, A. K. Geim, V. I. Fal'ko, and A. Mishchenko, *Nature (London)* **620**, 756 (2023).
- [122] D. Waters, E. Thompson, E. Arreguin-Martinez, M. Fujimoto, Y. Ren, K. Watanabe, T. Taniguchi, T. Cao, D. Xiao, and M. Yankowitz, *Nature (London)* **620**, 750 (2023).
- [123] L. Wang, S. Zihlmann, M.-H. Liu, P. Makk, K. Watanabe, T. Taniguchi, A. Baumgartner, and C. Schönenberger, *Nano Lett.* **19**, 2371 (2019).
- [124] R. Smeyers, M. V. Milošević, and L. Covaci, *Nanoscale* **15**, 4561 (2023).
- [125] P. Wang, Y. Zheng, X. Chen, C. Huang, Y. V. Kartashov, L. Torner, V. V. Konotop, and F. Ye, *Nature (London)* **577**, 42 (2020).
- [126] T. Salamon, A. Celi, R. W. Chhajlany, I. Frérot, M. Lewenstein, L. Tarruell, and D. Rakshit, *Phys. Rev. Lett.* **125**, 030504 (2020).
- [127] X.-W. Luo and C. Zhang, *Phys. Rev. Lett.* **126**, 103201 (2021).
- [128] Z. Meng, L. Wang, W. Han, F. Liu, K. Wen, C. Gao, P. Wang, C. Chin, and J. Zhang, *Nature (London)* **615**, 231 (2023).
- [129] L. C. Collins, T. G. Witte, R. Silverman, D. B. Green, and K. K. Gomes, *Nat. Commun.* **8**, 15961 (2017).
- [130] Y. Wang, Z. Ni, L. Liu, Y. Liu, C. Cong, T. Yu, X. Wang, D. Shen, and Z. Shen, *ACS Nano* **4**, 4074 (2010).
- [131] J. Yin, H. Wang, H. Peng, Z. Tan, L. Liao, L. Lin, X. Sun, A. L. Koh, Y. Chen, H. Peng, and Z. Liu, *Nat. Commun.* **7**, 10699 (2016).
- [132] N. C. H. Hesp, S. Batlle-Porro, R. K. Kumar, H. Agarwal, D. Barcons-Ruiz, H. H. Sheinflux, K. Watanabe, T. Taniguchi, P. Stepanov, and F. H. L. Koppens, [arXiv:2302.05487](https://arxiv.org/abs/2302.05487).
- [133] M. Oh, K. P. Nuckolls, D. Wong, R. L. Lee, X. Liu, K. Watanabe, T. Taniguchi, and A. Yazdani, *Nature (London)* **600**, 240 (2021).
- [134] H. Oka and M. Koshino, *Phys. Rev. B* **104**, 035306 (2021).
- [135] M. Koshino and H. Oka, *Phys. Rev. Res.* **4**, 013028 (2022).
- [136] M. K. Jat, P. Tiwari, R. Bajaj, I. Shitut, S. Mandal, K. Watanabe, T. Taniguchi, H. R. Krishnamurthy, M. Jain, and A. Bid, [arXiv:2304.01720](https://arxiv.org/abs/2304.01720).
- [137] W. Yao, E. Wang, C. Bao, Y. Zhang, K. Zhang, K. Bao, C. K. Chan, C. Chen, J. Avila, M. C. Asensio, J. Zhu, and S. Zhou, *Proc. Natl. Acad. Sci.* **115**, 6928 (2018).
- [138] P. Moon, M. Koshino, and Y.-W. Son, *Phys. Rev. B* **99**, 165430 (2019).
- [139] J. A. Crosse and P. Moon, *Phys. Rev. B* **103**, 045408 (2021).
- [140] M. J. Hamer, A. Giampietri, V. Kandyba, F. Genuzio, T. O. Menteş, A. Locatelli, R. V. Gorbachev, A. Barinov, and M. Mucha-Kruczyński, *ACS Nano* **16**, 1954 (2022).
- [141] S. L. Arlinghaus and W. C. Arlinghaus, *Geogr. Anal.* **21**, 103 (1989).
- [142] E. J. Mele, *Phys. Rev. B* **81**, 161405(R) (2010).
- [143] P. Coleman, in *Introduction to Many-Body Physics* (Cambridge University Press, New York, 2015), p. 71–94.
- [144] H. C. Po, L. Zou, A. Vishwanath, and T. Senthil, *Phys. Rev. X* **8**, 031089 (2018).
- [145] N. F. Q. Yuan and L. Fu, *Phys. Rev. B* **98**, 045103 (2018).
- [146] N. Marzari, A. A. Mostofi, J. R. Yates, I. Souza, and D. Vanderbilt, *Rev. Mod. Phys.* **84**, 1419 (2012).
- [147] G. Binnig, H. Rohrer, C. Gerber, and E. Weibel, *Phys. Rev. Lett.* **49**, 57 (1982).